arXiv:1303.5063v1 [astro-ph.IM] 20 Mar 2013

Planck 2013 results. II. The Low Frequency Instrument data processing

Planck Collaboration: N. Aghanim[59], C. Armitage-Caplan[90], M. Arnaud[73], M. Ashdown[70,6], F. Atrio-Barandela[18], J. Aumont[59], C. Baccigalupi[84], A. J. Banday[93,9], R. B. Barreiro[66], E. Battaner[95], K. Benabed[60,92], A. Benoît[57], A. Benoit-Lévy[26,60,92], J.-P. Bernard[9], M. Bersanelli[35,49], P. Bielewicz[93,9,84], J. Bobin[73], J. J. Bock[68,10], A. Bonaldi[69], L. Bonavera[66], J. R. Bond[7], J. Borrill[13,87], F. R. Bouchet[60,92], M. Bridges[70,6,63], M. Bucher[1], C. Burigana[48,33], R. C. Butler[48], B. Cappellini[49], J.-F. Cardoso[74,1,60], A. Catalano[75,72], A. Chamballu[73,15,59], X. Chen[56], L.-Y Chiang[62], P. R. Christensen[81,38], S. Church[89], S. Colombi[60,92], L. P. L. Colombo[25,68], B. P. Crill[68,82], M. Cruz[20], A. Curto[6,66], F. Cuttaia[48], L. Danese[84], R. D. Davies[69], R. J. Davis[69], P. de Bernardis[34], A. de Rosa[48], G. de Zotti[45,84], J. Delabrouille[1], C. Dickinson[69], J. M. Diego[66], H. Dole[59,58], S. Donzelli[49], O. Doré[68,10], M. Douspis[59], X. Dupac[40], G. Efstathiou[63], T. A. Enßlin[78], H. K. Eriksen[64], M. C. Falvella[5], F. Finelli[48,50], O. Forni[93,9], M. Frailis[47], E. Franceschi[48], T. C. Gaier[68], S. Galeotta[47], K. Ganga[1], M. Giard[93,9], G. Giardino[41], Y. Giraud-Héraud[1], E. Gjerløw[64], J. González-Nuevo[66,84], K. M. Górski[68,97], S. Gratton[70,63], A. Gregorio[36,47], A. Gruppuso[48], F. K. Hansen[64], D. Hanson[79,68,7], D. Harrison[63,70], S. Henrot-Versillé[71], C. Hernández-Monteagudo[12,78], D. Herranz[66], S. R. Hildebrandt[10], E. Hivon[60,92], M. Hobson[6], W. A. Holmes[68], A. Hornstrup[16], W. Hovest[78], K. M. Huffenberger[96], T. R. Jaffe[93,9], A. H. Jaffe[55], J. Jewell[68], W. C. Jones[28], M. Juvela[27], P. Kangaslahti[68], E. Keihänen[27], R. Keskitalo[23,13], K. Kiiveri[27,43], T. S. Kisner[77], J. Knoche[78], L. Knox[29], M. Kunz[17,59,3], H. Kurki-Suonio[27,43], G. Lagache[59], A. Lähteenmäki[2,43], J.-M. Lamarre[72], A. Lasenby[6,70], R. J. Laureijs[41], C. R. Lawrence[68], S. Leach[84], J. P. Leahy[69], R. Leonardi[40], J. Lesgourgues[91,83], M. Liguori[32], P. B. Lilje[64], V. Lindholm[27,43], M. Linden-Vørnle[16], M. López-Caniego[66], P. M. Lubin[30], J. F. Macías-Pérez[75], G. Maggio[47], D. Maino[35,49], N. Mandolesi[48,5,33], M. Maris[47], D. J. Marshall[73], P. G. Martin[7], E. Martínez-González[66], S. Masi[34], S. Matarrese[32], F. Matthai[78], P. Mazzotta[37], P. R. Meinhold[30], A. Melchiorri[34,51], L. Mendes[40], A. Mennella[35,49], M. Migliaccio[63,70], S. Mitra[54,68], A. Moneti[60], L. Montier[93,9], G. Morgante[48], D. Mortlock[55], A. Moss[86], D. Munshi[85], P. Naselsky[81,38], P. Natoli[33,4,48], C. B. Netterfield[21], H. U. Nørgaard-Nielsen[16], D. Novikov[55], I. Novikov[81], I. J. O'Dwyer[68], S. Osborne[89], F. Paci[84], L. Pagano[34,51], R. Paladini[56], D. Paoletti[48,50], B. Partridge[42], F. Pasian[47], G. Patanchon[1], M. Peel[69], O. Perdereau[71], L. Perotto[75], F. Perrotta[84], E. Pierpaoli[25], D. Pietrobon[68], S. Plaszczynski[71], P. Platania[67], E. Pointecouteau[93,9], G. Polenta[4,46], N. Ponthieu[59,52], L. Popa[61], T. Poutanen[43,27,2], G. W. Pratt[73], G. Prézeau[10,68], S. Prunet[60,92], J.-L. Puget[59], J. P. Rachen[22,78], W. T. Reach[94], R. Rebolo[65,14,39], M. Reinecke[78], M. Remazeilles[59,1], S. Ricciardi[48], T. Riller[78], G. Rocha[68,10], C. Rosset[1], G. Rossetti[35,49], G. Roudier[1,72,68], J. A. Rubiño-Martín[65,39], B. Rusholme[56], E. Salerno[8], M. Sandri[48], D. Santos[75], D. Scott[24], M. D. Seiffert[68,10], E. P. S. Shellard[11], L. D. Spencer[85], J.-L. Starck[73], V. Stolyarov[6,70,88], R. Stompor[1], F. Sureau[73], D. Sutton[63,70], A.-S. Suur-Uski[27,43], J.-F. Sygnet[60], J. A. Tauber[41], D. Tavagnacco[47,36], L. Terenzi[48], L. Toffolatti[19,66], M. Tomasi[49], M. Tristram[71], M. Tucci[17,71], J. Tuovinen[80], M. Türler[53], G. Umana[44], L. Valenziano[48], J. Valiviita[43,27,64], B. Van Tent[76], J. Varis[80], P. Vielva[66], F. Villa[48], N. Vittorio[37], L. A. Wade[68], B. D. Wandelt[60,92,31], R. Watson[69], I. K. Wehus[68], S. D. M. White[78], A. Wilkinson[69], D. Yvon[15], A. Zacchei[47] *, and A. Zonca[30]

(Affiliations can be found after the references)

Preprint online version: March 22, 2013

ABSTRACT

We describe the data processing pipeline employed by the Low Frequency Instrument (LFI) data processing centre (DPC) to create and characterize the full-sky maps based on the first 15.5 months of operations at 30, 44 and 70 GHz. In particular, we discuss the various steps involved in reducing the data, starting from telemetry (TM) packets through to the production of cleaned calibrated timelines and calibrated frequency maps. Data are continuously calibrated using the modulation induced on the mean temperature of the cosmic microwave background radiation by the proper motion of the spacecraft. Sky signals other than the dipole are removed by an iterative procedure based on simultaneous fitting of calibration parameters and sky maps. Noise properties are estimated from time-ordered data after the sky signal has been removed, using a generalized least square map-making algorithm. A destriping code (`Madam`) is employed to combine radiometric data and pointing information into sky maps, minimizing the variance of correlated noise. Noise covariance matrices, required to compute statistical uncertainties on LFI and *Planck* products, are also produced. Main beams are estimated down to the ≈ -20 dB level using Jupiter transits, which are also used for the geometrical calibration of the focal plane.

Key words. methods:data analysis; cosmology: cosmic microwave background

1. Introduction

This paper, one of a set associated with the 2013 release of data from the *Planck*[1] mission (Planck Collaboration I 2013),

---

describes the LFI (low frequency instrument) data processing which supports the first *Planck* cosmological release based on the nominal *Planck* survey (15.5 months of observation). This paper represents an updated version of the LFI data processing description (Zacchei et al. 2011) which was part of the first wave of early astrophysical results published in early 2011 (Planck Collaboration, 2011h-z). This work describes the over-

telescope reflectors provided by a collaboration between ESA and a scientific consortium led and funded by Denmark.

all data flow of the pipeline implemented at the LFI DPC, from instrument scientific telemetry and housekeeping data to frequency maps, as well as the test plan applied to validate the data products. Due to the complexity of the analysis process, three companion papers and one explanatory document will provide further details on specific critical aspects of the data analysis and products delivered, and they will be referenced here as appropriate. In Planck Collaboration III (2013) we discuss systematic effects in detail and present an overall error budget. In Planck Collaboration V (2013) we describe photometric calibration, and provide details of the methods implemented and the related uncertainties. Next the determination of the detector main beams and their uncertainties, based on in-flight planet-crossing measurements, is presented in Planck Collaboration IV (2013). Finally in Planck Collaboration ES (2013) description of the products delivered is detailed. When needed, the justification for the choice of the algorithm used in the pipeline will be discussed in the relevant companion papers. All the main information and reference tables discussed in detail in companion papers (e.g., noise characterization, beam parameters, etc.) will, however, be reported and summarized in this work.

2. LFI in-flight behaviour and operations

The *Planck* LFI instrument is described in detail in Bersanelli et al. (2010) and Mennella et al. (2010). It comprises eleven Radiometer Chain Assemblies (RCA's), two at 30 GHz, three at 44 and six at 70 GHz, each composed of two independent pseudo-correlation radiometers sensitive to orthogonal linear polarizations. Each radiometer has two independent square-law diodes for detection, integration and conversion from RF signal into DC voltages. The LFI focal plane is cryogenically cooled to 20 K, while the pseudo-correlation design uses internal, black-body, reference loads cooled to ~ 4.5 K (4KRL). The radiometer timelines are produced by taking differences between the signals from the sky, V_{sky}, and from the reference loads, V_{ref}. Radiometer balance is optimized by introducing a gain modulation factor, typically stable within 0.04% throughout the mission, which greatly reduces $1/f$ noise and improves immunity to a wide class of systematic effects (see Mennella et al. 2011, for further details). During the entire nominal survey, the behavior of all 22 LFI radiometers was highly stable, with $1/f$ knee frequencies of order 50 mHz and white noise levels unchanging within 0.5%. Because of the stability of the instrument, only a very limited number of corrections were required in the LFI data processing, either at the TOI (time ordered information) and map level.

2.1. Operations

During the period of observation the entire satellite was very stable (Planck Collaboration I 2013), with a single exception. Three months before the end of the nominal mission it was necessary, as scheduled, to switch from the nominal to the redundant sorption cooler. This operation, briefly described below, was visible in the LFI scientific data, but the effect on the temperature power spectrum was estimated to be negligible (see Sect. 2.2)

2.2. Switch-over from nominal to redundant Sorption Cooler

The 20 K cooling on *Planck* is provided by the sorption cooler system (SCS). This cooler uses six metal hydride compressor elements to produce high-pressure hydrogen that is circulated

through a Joule-Thomson valve to provide 1 W of cooling at 20 K. Gas compression is achieved by heating a single compressor element to 440 K and a pressure of 30 Bar. After expansion through the Joule-Thomson valve, the gas is recovered by three compressor elements at 270 K and 0.3 Bar. To reduce power consumption, gas-gap heat switches are used to isolate the compressor elements from the radiator during gas compression. Two sorption coolers were flown on the *Planck* spacecraft to meet mission lifetime requirements. A *switchover* procedure was developed to change between the operating cooler and the redundant cooler. In early August of 2010, one of the gas-gap heat switches for a compressor element failed on the active cooler. Although the SCS can operate with as few as four compressor elements, it was decided to implement the switchover procedure and activate the redundant cooler. On 11 August at 17:30 GMT, the working cooler was commanded off, and the redundant cooler was switched on. Adequate cryogenic cooling was restored in about 1 hour. Return to thermal stability, however, took 48 hours. After thermal stability of the SCS was restored, anomalous temperature fluctuations were observed on the LFI focal plane. These excess fluctuations are thought to be due to sloshing of liquid hydrogen remaining in the cooler that had been switched off. This was due to the loss of storage capacity of the metal hydride of the inactive cooler, which prevented a reduction of the pressure to a level that prevented liquid formation. While these fluctuations produced a measurable effect in the LFI data, their propagation to the temperature power spectrum is more than two orders of magnitude below the CMB signal (Planck Collaboration III 2013). Furthermore, after the end of the nominal mission in February 2011, these fluctuations were reduced to a much lower level. More details of these issues will be discussed in a future paper.

2.3. Instrument performance update

Table 1 gives a top-level summary of instrument performance parameters measured in flight during the nominal data period. Optical properties have been successfully reconstructed using Jupiter transits (Planck Collaboration IV 2013) and the main parameters are in agreement with pre-launch and early estimates (Mennella et al. 2011). The white noise sensitivity and parameters describing the $1/f$ noise component are in line with ground measurements (Mennella et al. 2010) and agree with the values published in the early paper (Mennella et al. 2011) Photometric calibration based on the CMB dipole, yields an overall statistical uncertainty of 0.25% (Planck Collaboration V 2013). Variations due to slow instrumental variations are traced by the calibration pipeline, yielding an overall uncertainty ranging between 0.1% and 0.2%. The residual systematic uncertainty is linked to the frequency and varies between 21 muK and $6 \mu K_{CMB}$ (Planck Collaboration III 2013).

3. LFI Data processing overview

The processing of LFI data can be logically divided into a series of levels shown schematically in Fig. 1. The process starts with the Level 1 (L1); this has the responsibility to retrieve all necessary information from packets and auxiliary data received each day from the Mission Operation Center and to transform the scientific packets and housekeeping data into a form that is manageable by the Level 2 (L2) scientific pipeline. The Level 2 pipeline queries the database where the L1 data has been stored and, using scientific and housekeeping information, does the following

Table 1. Summary of main LFI performance parameters.

Parameter	30 GHz	44 GHz	70 GHz
Centre frequency [GHz]	28.4	44.1	70.4
Scanning Beam [a] FWHM [']	33.16	28.09	13.08
Scanning Beam [a] Ellipticity	1.37	1.25	1.27
Effective Beam [b] FWHM [']	32.34	27.12	13.31
White noise sensitivity (map level) [c] [μK_{CMB}]	9.2	12.5	23.2
White noise sensitivity (from timelines)[$\mu K_{CMB} s^{1/2}$]	148.5	173.2	151.9
f_{knee} [mHz]	114.5	45.7	20.2
$1/f$ slope	−0.92	−0.90	−1.13
Overall calibration uncertainty [%]	0.82	0.55	0.62
Systematic effects uncertainty [μK_{CMB}]	21.02	5.61	7.87

[a] FWHM and ellipticity from scanning beam evaluated fitting Jupiter directly in the timelines.

[b] FWHM from effective beam estimated from the main beam solid angle of the effective beam, see Sec. 6.2. Those are the values used in the source extraction pipeline (Planck Collaboration XXVIII 2013).

[c] White noise per pixel computed from half-ring difference maps. Those values are within the 1% with the white noise sensitivity computed directly on the timelines, taking in account the actual mission time minus the manoeuvres and bad-science flagged data.

- build the LFI RIMO (reduced instrument model) that contains all the main characteristics of the instrument;
- remove AD/C non linearity and 1 Hz spikes at diode level (see Sects. 4.2 and 4.3);
- compute and apply the gain modulation factor to minimize the $1/f$ noise (see Sect. 4.4);
- combine the signals from the diodes (see Sect. 4.5);
- compute the corresponding detector pointing for each sample, based on auxiliary data and beam information (see Sect. 5);
- calibrate the scientific timelines to physical units (K_{CMB}) fitting the dipole convolved with the 4π beam representation (see Sect. 7);
- remove from the scientific calibrated timeline the dipole convolved with the 4π beam representation;
- combine the calibrated TOIs into aggregate products such as maps at each frequency (see Sect. 9).

The Level 3 collects instrument-specific (from both HFI and LFI) L2 outputs and derives various products. For instance, component-separation algorithms transform frequency maps into maps of separated astrophysical components; source detection algorithms create catalogues of different classes of object and sources; and finally a likelihood code assesses the match between a cosmological and astrophysical model, on the one hand, and the frequency maps on the other.

4. Time ordered information (TOI) processing

In the L1 pipeline the telemetry data are received at the DPC (data processing center) as a stream of packets which are handled automatically by different steps in the Level 1:

- uncompress the retrieved packets;
- de-quantize and de-mix the uncompressed packets to retrieve the original signal in ADU (analog-to-digital units);
- using a conversion factor stored in the packet header to transform ADU data in to volts;
- cross correlate time information to univocally time stamp each sample;
- store the resulting timelines into a database interface to the Level 2 pipeline.

We made no change in Level 1 software during the mission. Detailed information on how each of the steps listed above were applied is provided in the early paper by Zacchei et al. (2011). In order to avoid strong gradients in the signal and signals that do not project correctly in the maps, we establish a procedure able to flag a single scientific sample; this is described in Sect. 4.1.

4.1. Input flags

For each sample we define a 32-bit flag mask to identify potential inconsistencies in the data and to enable the pipeline to skip that sample or handle it differently. The TOI from all LFI detectors is archived in the Level 1 database, and regularly checked to identify and flag events that can affect the scientific analysis. These events include missing or anomalous data, and data acquired during the manoeuvres regularly performed to repoint the telescope according to the *Planck* scanning strategy. Table 2 summarizes, for the period of the nominal mission, the percentage of time associated with these events in the LFI TOIs. The table also reports the total percentage of Level 1 TOIs usable in the scientific analysis. Most of the missing data results from telemetry packets where the arithmetic compression performed by the SPU is incorrect, causing a decompression error. They are very rare, and hence they cause a completely negligible impact on the scientific analysis. For instance, for the entire 70 GHz frequency channel, the total amount of missing data corresponds to 130 lost seconds in 15 months. The instrument team performs a daily check of the LFI data retrieved during the daily tele-communication period with the satellite; the data covers an entire operational day. Part of this analysis consists in identifying, for each LFI detector, time windows where either the total power signal or the differentiated signal shows anomalous fluctuations or jumps. Depending on the characteristics of the anomaly identified, a time window can be flagged as unusable for science. Currently, the criteria defined to flag time windows as unusable include:

- time windows where a gain change in the data acquisition electronics caused a saturation of the sky or reference load signals;
- abrupt changes in voltage output with slow recovery (>1 m), caused by gain fluctuations in the back-end module ampli-
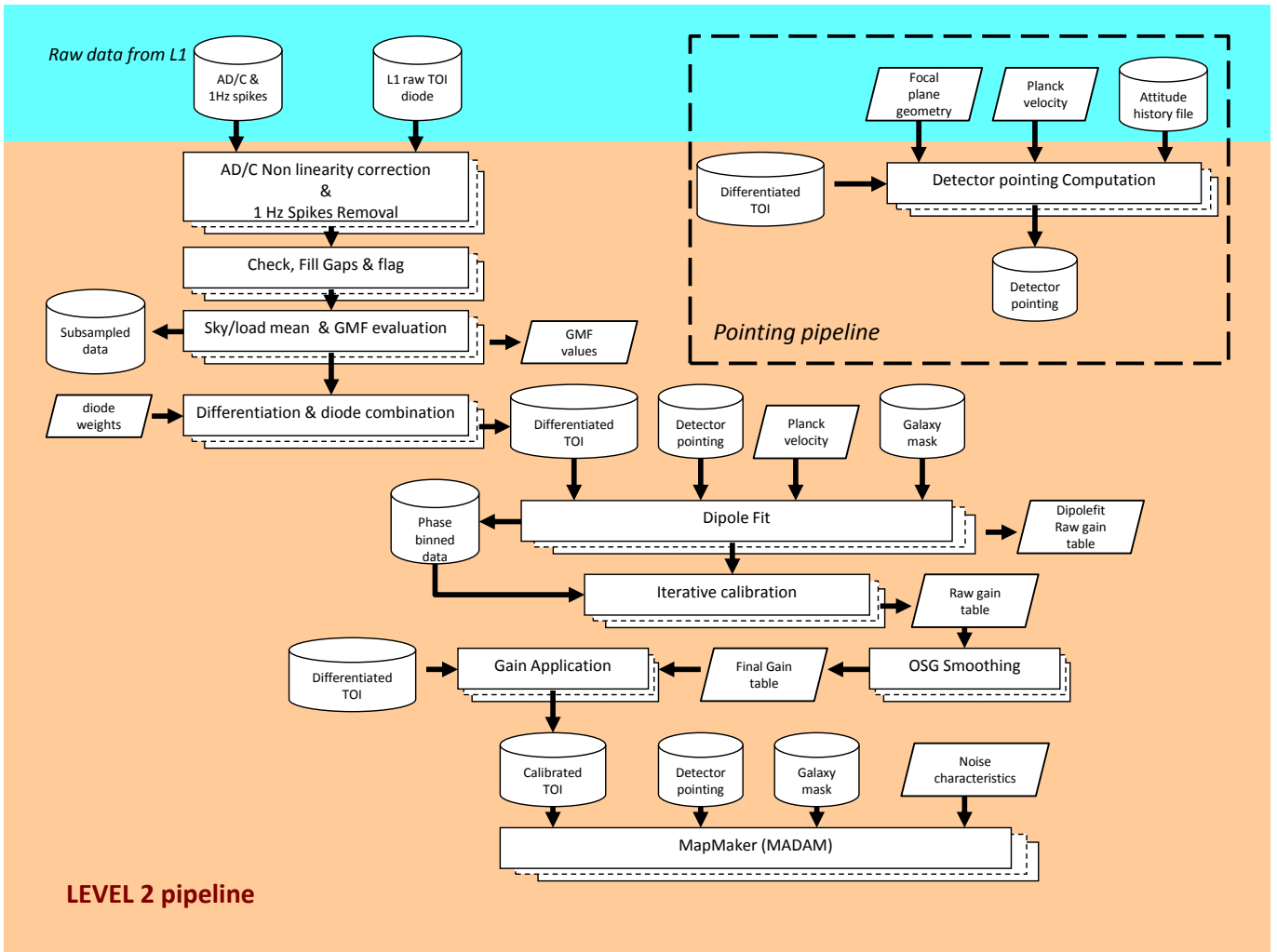
Fig. 1. Schematic representation of Level 1, Level 2 and pointing pipeline of LFI DPC

fier, induced by electrical or thermal variations, which also generate discontinuities in the differentiated signal;

– short, abrupt changes in voltage output caused by fluctuations in the low noise amplifiers in the front end module, which produce asymmetries between the sky and reference load signals and possibly first order effects in the differentiated signal;

– permanent changes in the output voltage caused by a permanent change at the front end module (amplifier bias or focal plane unit temperature) or back end module (temperature or HEMT gain variations); in such cases, only a small time window around the discontinuity is flagged as unusable;

– short time windows (<1 m) where the total power signal shows pop-corn noise on one or both detectors, due to variations in the bcd end diode or in the front end low noise amplifiers

In Table 2, the row labelled as "Anomalies" reports the percentage of observation time flagged as unusable for these reasons in the scientific analysis. The almost 1.0% shown for the 44 GHz channel corresponds to a total time of 113 hours. Finally, the times of manoeuvres and stable pointing periods are recovered from the attitude history files provided by the *Planck* flight dynamics team. Detector samples corresponding to manoeuvres are flagged out, in order to skip them during the present analysis.

Table 2. Summary of the percentage of the LFI observation time spent in manoeuvres, lost due to missing or unusable data and effectively used in the scientific analysis, calculated by frequency channel.

	30 GHz	44 GHz	70 GHz
Missing [%]	0.00014	0.00023	0.00032
Anomalies [%]	0.82220	0.99763	0.82925
Maneuvers [%]	8.07022	8.07022	8.07022
Usable [%]	91.10744	90.93191	91.10021

Tasks within the Level 2 pipelines both fill gaps in the data with artificial noise and flag them properly. Other tasks locate planet transits and moving objects within the Solar system, again flagging samples affected by such observations.

4.2. ADC linearity correction

The analogue to digital converters are the part of the data acquisition electronics responsible for producing the digital presentations of the analogue detector voltages which are then processed on-board by the radiometer electronics box assembly. Since they are directly involved with the signal power, their linearity is as important as that of the receivers and detectors, with any de-

parture appearing as a distortion in the system power response curve. In differential measurements such as those carried out by the *Planck* LFI instrument, very small localized glitches in this curve can have a large impact, since the calibration factor depends on the gradient of the response curve at the point at which the differential measurements are made. This effect is described in detail in the systematics paper Planck Collaboration III (2013) and the impact on calibration in Planck Collaboration V (2013).

The effect is observed in some LFI radiometer data, appearing as gain variations seen at particular detector voltages. This is shown for the worst affected channel RCA2501, in Fig. 2, where the upper plot shows the measured voltages of the sky and reference loads (in red and blue respectively) and the lower plot the percentage variations of gain (green) and noise on sky and reference voltages (red and blue). The range of the upper plot is matched to that of the lower plot and so for normal gain variations the same pattern should be seen for both. That is clearly not the case. When the sky signal falls close to 0.186 V, as shown by the horizontal dashed lines, both the inverse gain and the sky "white noise" estimates show anomalies in the same time interval (the time interval affected is indicated by vertical dashed lines in the Fig. 2). The same anomalous behavior of the reference "white noise" signal and inverse gain is seen in two intervals when the reference signal falls close to either 0.197 V or 0.202 V. Outside of these limited ranges, the variations in all plotted signals track one another, such as the feature at 192 days after launch in the sky voltage or the drop at day 257 when the transponder was turned permanently on.

The response curves can be reconstructed by tracking how the noise amplitude varies with the apparent detector voltage in the TOI. The radiometers are assumed to be stable and the intrinsic thermal noise can be taken to be constant in terms of temperature, so any voltage variations are then assumed to be due to both gain drift and ADC effects. The method for this correction is set out in appendix A of Planck Collaboration III (2013).

4.3. Corrections for electronic spikes

This effect is caused by interaction between the housekeeping electronics clock and the scientific data line in the on-board data acquisition system. The spikes are synchronous with the on-board time with no changes in phase over the entire acquisition period, allowing the construction of dedicated templates that are then removed from the timelines. Frequency spikes are present in the output at all frequency but affect mostly the 44 GHz due to the high gain in these detectors: consequently, electronic spikes are removed only in this channel. This process and the evaluation of the effect at map level is described in Planck Collaboration III (2013).

4.4. Demodulation: Gain modulation factor estimation and application

Each diode switches at 4096 Hz (Mennella et al. 2010) between the sky, V_{sky}, and the 4 K reference load, V_{load}. V_{sky} and V_{load} are dominated by $1/f$ noise, with knee frequencies of tens of hertz. This noise is highly correlated between the two streams, a result of the pseudo-correlation design (Bersanelli et al. 2010), and differencing the streams results in a dramatic reduction of the $1/f$ noise. To force the mean of the difference to zero, the load signal is multiplied by the GMF (gain modulation factor), R, which can be computed in several ways (Mennella et al. 2003). The simplest method, and the one implemented in the process-
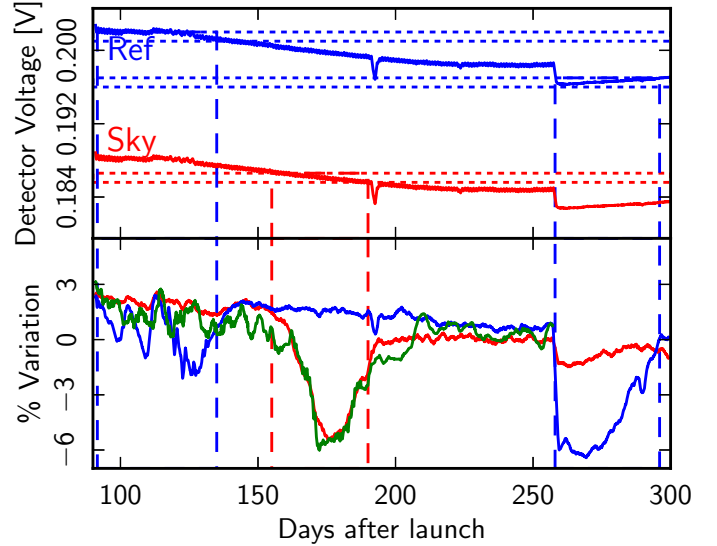

Fig. 2. Effect of ADC non-linearities on time ordered data of one of the 44 GHz diode. The upper plot shows the recorded detector voltage (sky in red and reference in blue). The horizontal shaded bars show the voltage range affected by the ADC non-linearities and the vertical bars the time range affected. The lower plot shows the percentage variation of the inverse of the gain factor from the dipole gain (green) and the "white noise" estimates on the sky and reference voltages (again sky red and reference blue). The gain estimates have been smoothed by a three day moving mean and the noise by one day.

ing pipeline, is to take the ratio of DC levels from sky and load outputs obtained by averaging the two time streams, i.e., $R = \langle V_{sky} \rangle / \langle V_{load} \rangle$. Then

$$\Delta V(t) = V_{sky}(t) - \frac{\langle V_{sky} \rangle}{\langle V_{load} \rangle} V_{load}(t) \,. \tag{1}$$

The R value was computed from unflagged data for each pointing period and then applied to create the differenced timelines. The R factor has been stable over the mission so far, with overall variations of 0.03–0.04 %. Full discussion regarding the theory of this value is reported in Mennella et al. (2011)

4.5. Combining diodes

The receiver architecture is symmetric, with two complementary detector diodes providing output for each receiver channel. As described in Seiffert et al. (2002) and Mennella et al. (2010), imperfect matching of components limits the isolation between the complementary diodes of the receivers to between -10 and -15 dB. This imperfect isolation leads to a small anti-correlated component in the white noise. We perform a weighted average of the time ordered data from the two diodes of each receiver just before the differentiation. This avoids the complication of tracking the anticorrelated white noise throughout the subsequent analysis. We treat the combined diode data as the raw data, and calibration, noise estimation, mapmaking etc. are performed on these combined data. We use inverse noise weights determined from an initial estimate of the calibrated noise for each detector. The weights, reported in Table 3, are kept fixed for the entire mission.

Table 3. Diode weights applied (first three decimals), perfect instrument would have 0.500 weights for both diodes.

	M-00	M-01	S-10	S-11
LFI18	0.567	0.433	0.387	0.613
LFI19	0.502	0.498	0.551	0.449
LFI20	0.523	0.477	0.477	0.523
LFI21	0.500	0.500	0.564	0.436
LFI22	0.536	0.464	0.554	0.446
LFI23	0.508	0.492	0.362	0.638
LFI24	0.602	0.398	0.456	0.544
LFI25	0.482	0.518	0.370	0.630
LFI26	0.593	0.407	0.424	0.576
LFI27	0.520	0.480	0.485	0.515
LFI28	0.553	0.447	0.468	0.532

5. Pointing

Proper pointing reconstruction is critical and has a direct impact in the determination of an accurate photometric calibration. The pointing for each radiometer $\hat{\boldsymbol{P}}_{\mathrm{rad}}(t)$ at time t is given by

$$\hat{\boldsymbol{P}}_{\mathrm{rad}}(t) = \mathcal{R}_{\mathrm{Ecl,Body}}(t)\mathcal{R}_{\mathrm{Body,rad}}\hat{\boldsymbol{e}}_{\mathrm{z}}. \tag{2}$$

The $\mathcal{R}_{\mathrm{Body,rad}}$ matrix encodes the orientation of the beam pattern with respect to the body reference frame, i.e., the reference frame defined by the spacecraft structure. We adopt the convention that in the reference frame of the beam the optical axis is aligned with $\hat{\boldsymbol{e}}_{\mathrm{z}}$. The $\mathcal{R}_{\mathrm{Body,rad}}$ is parameterized by a set of rotation angles in the RIMO derived from flight data and ground based measurements. The $\mathcal{R}_{\mathrm{Ecl,Body}}(t)$ is derived by time interpolation of quaternions distributed in the attitude history files. The spacecraft attitude is determined by the *Planck* Star Tracker and during periods of stability between maneuvers is sampled at 8 Hz, much lower than the LFI sampling frequency. Despite its simplicity, this formula synthesizes a large amount of information on the satellite and a long chain of transformations between reference frames, each one being a possible source of systematic errors. Indeed, even a small aberration compared to the beam size can introduce significant photometric effects if the gradient of the temperature field is large enough. The two most important sources of aberration identified and corrected in *Planck*/LFI are stellar aberration and the apparent change in wobble angles likely produced by thermal deformations of the star tracker support.

5.1. Stellar Aberration

The star tracker system provides reconstructed astrometric attitude for the *Planck* spacecraft in the Solar System baricentric reference frame (SSB). However the effective pointing direction is aberrated by the well known effect of orbital stellar aberration due to the combination of *Planck* orbital motion and finite speed of light. In the non-relativistic case stellar aberration follows the well known equation

$$\hat{\boldsymbol{P}}' = (\hat{\boldsymbol{P}} + \mathbf{v}_{\mathrm{Planck}}/c)/\left|\hat{\boldsymbol{P}} + \mathbf{v}_{\mathrm{Planck}}/c\right|, \tag{3}$$

where $\hat{\boldsymbol{P}}'$ is the aberrated pointing direction, $\mathbf{v}_{\mathrm{Planck}}$ is the orbital velocity of *Planck* in the SSB reference frame, and c the speed of light. From this formula the deflection angle $\delta_{\mathrm{P}} = \arccos \hat{\boldsymbol{P}}' \cdot \hat{\boldsymbol{P}}$ can be derived. Since *Planck* moves at about 30 Km s^{-1} in the Solar System, its motion is nearly coplanar to the ecliptic and

scan circles are nearly normal to it: $\delta_{\mathrm{P}} \leq 20.6''$, the worst deflection occurs near the ecliptic poles. If left uncorrected, this aberration would distort the maps and it will be more similar to a seasonal shift near the equator and to a "blurring" near the ecliptic poles. Indeed a set of accurate simulations shows that the distortion radius is maximal at the ecliptic poles, i.e., at mid Galactic latitudes $(l_{\mathrm{Gal}}, b_{\mathrm{Gal}}) = (96.384°, 29.811°)$ and $(l_{\mathrm{Gal}}, b_{\mathrm{Gal}}) = (276.384°, -29.811°)$, and that it decreases toward the ecliptic down to a minimum of about $0.1°$ on the ecliptic. The boundary of the worst affected region, i.e., the region in which the distortion radius is at least half the polar value, is roughly a ring centred on the poles with radius about $60°$. There are some variations in the radius and in the longitudinal shape of the boundary, both smaller than a few degrees, due to the scanning strategy and also to the different angular distances from the spin axis of the various feed–horns.

5.2. Wobble Angles

Wobble angles describe the unavoidable misalignment of the body reference frame with respect to the reference frame defined by the satellite principal inertial axis. The nominal spin axis for the satellite is nearly a half degree away from the principal moment of inertia and the effective scan circles are about half a degree smaller than the nominal ones (Planck Collaboration I 2011). Wobble angles and their variations in time, either real or apparent, are measured by careful modelling of the observed *Planck* attitude dynamics included in the attitude history files. Planck Collaboration I (2011) reported an apparent variation of the wobble angles likely produced by thermoelastic deformations which change the relative orientation of the star tracker with respect to the body reference frame. The change was detected in scans of Jupiter. Since this variation is rigidly transported by the rotations of spacecraft body, its effect will be largely averaged out near the poles and will be maximal near the ecliptic, the opposite of the stellar aberration effect. Of the three angles that describe the wobble, ψ_1 has largely negligible effects and ψ_3 is badly determined, so the LFI pipeline applies a correction for only the ψ_2 variation. Its effect is like an apparent change of the angular distance between the telescope and the spin axis so that a spurious change of this angle will be equivalent to an apparent change of scan circles radii of $\pm 0.1'$, giving an equivalent displacement in pointing between consecutive surveys of $0.2'$.

6. Main Beams and the geometrical calibration of the Focal Plane

Through measurements of Jupiter crossing we are able to measure the beam profiles (Planck Collaboration IV 2013) and directions. We use this information to determine the focal plane geometry, which is the pointing direction and its related polarization for each beam centre in the field of view. The origin of the focal plane is taken to coincide with the optical line of sight defined in Tauber et al. (2010). In the LFI RIMO the centre of beam is expressed by four numbers, namely θ_{uv}; ϕ_{uv}; ψ_{uv}; $\psi_{\mathrm{p}ol}$; see Planck Collaboration ES (2013) for the definition of these angles. Only θ_{uv} and ϕ_{uv}, which are the beam pointing in spherical coordinates referred to the line of sight, can be determined with Jupiter observations; the polarization orientation of the beams, defined by $\psi_{\mathrm{uv}} + \psi_{\mathrm{p}ol}$, is not estimated from flight data but is derived from main beam simulations based on ground measurements.

Table 4. Approximate dates of the Jupiter observations.

Jupiter crossing	Date	OD
Scan J1	21/10/09 – 05/11/09	161 – 176
Scan J2	27/06/10 – 12/07/10	410 – 425
Scan J3	03/12/10 – 18/12/10	569 – 584
Scan J4	30/07/11 – 08/08/11	808 – 817

The calibration of the beams and their locations was accomplished using the four Jupiter crossings which occurred in the periods reported in Table 4, following the same procedure already described in Zacchei et al. (2011) and Mennella et al. (2011).

For each beam, the pointing is determined by the location of the maximum of the elliptical Gaussian fit to that beams. This was done for each beam in each single scan whose results are reported, with errors, in Planck Collaboration IV (2013).

In addition, the beams were stacked in pairs (J1J2 and J3J4) and all together (J1J2J3J4) in order to improve the signal to noise ratio of the measurements. Before the stacking each beam was artificially repointed along the direction given by the arithmetic average of the centre of each single beam to be stacked. Then a fit was performed again on the stacked beams and the resulting parameters recorded. For single scans it has been found that there is an agreement within 2″ in the pointing direction between J1 and J2. The same agreement occurs between J3 and J4. In contrast, a ∼ 15″ systematic deviation of the beam centre was detected when comparing J1J2 to J3J4. Figure 3 reports the reconstructed beam positions and errors in the line of sight frame both magnified by a factor of 100. The shift is evident for the 70 GHz beams as well as in all the J1J2 and J3J4 stacked beam centres. It became manifest when we stacked the beams to improve the determination of their centres. The change in the location has been found mainly in the scan direction (i.e., *v*-coordinate). To account for this pointing shift we apply two pointing solutions for LFI. The first focal plane calibration is valid from OD91 to OD540 and it is based on the J1J2 beam pointing determination. The second calibration is valid from OD541 to OD563 and it is based on the J3J4 beam pointing calibration. The reconstructed angles are reported in Table 5

6.1. Scanning beams

Scanning beams are defined as the measured beams in flight. They include the smearing effect due to the satellite spinning, and the effects of the radiometers, such as the band shape. With four Jupiter transit measurements we were able to reconstruct the beam shape down to −20 dB from peak at 30 and 44 GHz, and down to −25 dB at 70 GHz. From the beam shape we estimated the main beam parameters using a bivariate Gaussian fit on the four stacked beams (J1J2J3J4). The fitting procedure, described in Zacchei et al. (2011), was slightly modified to correct for offset in the data and to avoid noise contamination. We refer to the companion paper on LFI beams (Planck Collaboration IV 2013) for details on procedures and results. Here we report in Table 6 the average values of the FWHM and ellipticity with errors.

6.2. Effective Beams

The effective beam is the average of all scanning beams pointing at a certain direction within a given pixel of the sky map with the *Planck* scanning strategy applied. We compute the effective

beam at each LFI frequency scanning beam and scan history in real space using the FEBeCoP (Mitra et al. 2011) method. Details of the application of FEBeCoP to *Planck* data will be discussed in a future paper. Effective beams were used to calculate the effective beam window function as reported in Planck Collaboration IV (2013) and in the source detection pipeline necessary to generates the PCCS catalogue (Planck Collaboration XXVIII 2013) We list in Table 7 the main parameters computed with FEBeCoP, Note that the FWHM and ellipticity in Table 7 differs slightly from the values reported in Table 6; this results from the different way in which the Gaussian fit was applied. The scanning beam fit was determined by fitting the profile of Jupiter on timelines and limiting the fit to the data with a signal above the 3σ level from the noise, while the fit of the effective beam was computed on GRASP maps projected in several position of the sky (Planck Collaboration IV 2013); the latter are less affected by the noise.

7. Photometric Calibration

In this section we discuss the procedures used to perform a photometric calibration of the *Planck*/LFI radiometric data, that is, the conversion of the time-ordered streams of voltages into time-ordered streams of thermodynamic temperatures. The conversion is modelled by the following equation:

$$V = G \times (T_{sky} + T_{noise}), \tag{4}$$

which relates the voltage V measured by the ADC with the temperature T_{sky}, obtained by convolving the sky temperature with the beam response of the instrument at a given time, and the noise temperature T_{noise} of the radiometer. In general we are interested in $K = G^{-1}$, as the purpose of the calibration is to convert V back into a temperature. As described in Planck
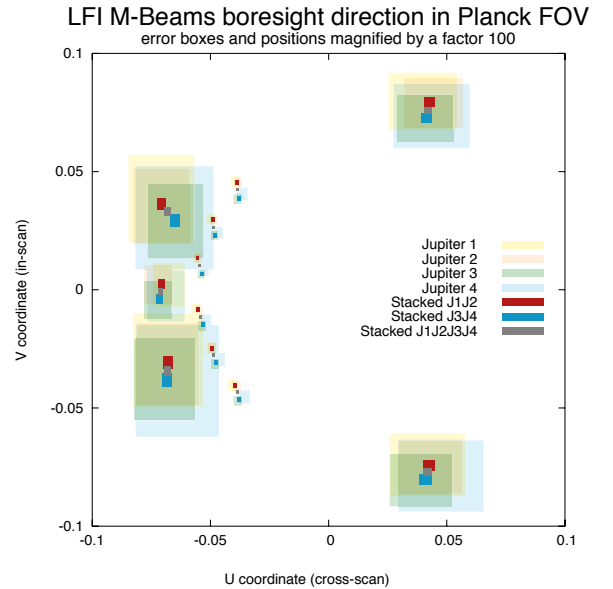

Fig. 3. Main beam pointing directions measured with the first four Jupiter crossings: single scans (yellow, light red, green, light blue); first and second stacked scans (red); third and fourth stacked scans (blue); and four stacked scans (grey) are reported. The colored boxes refer to the measured uncertainties magnified by a factor of 100. The differences in pointing were normalized to the J1 measurements, and were magnified by the same factor of 100.

Table 5. Focal plane geometry

Radiometer	$\theta_{uv}{}^a$	$\phi_{uv}{}^a$	$\theta_{uv}{}^b$	$\phi_{uv}{}^b$	$\psi_{uv}{}^c$	$\psi_{pol}{}^c$
LFI18S	3.334	−131.803	3.335	−131.752	22.200	0.000
LFI18M	3.333	−131.812	3.335	−131.759	22.200	90.200
LFI19S	3.208	−150.472	3.209	−150.408	22.400	0.000
LFI19M	3.208	−150.467	3.209	−150.402	22.400	90.000
LFI20S	3.183	−168.189	3.183	−168.121	22.400	0.000
LFI20M	3.183	−168.178	3.183	−168.109	22.400	89.900
LFI21S	3.184	169.265	3.182	169.324	−22.400	0.000
LFI21M	3.184	169.274	3.183	169.336	−22.400	90.100
LFI22S	3.172	151.352	3.170	151.405	−22.400	0.100
LFI22M	3.172	151.345	3.170	151.398	−22.400	90.100
LFI23S	3.280	132.255	3.277	132.287	−22.100	0.000
LFI23M	3.280	132.234	3.277	132.274	−22.100	89.700
LFI24S	4.070	−179.506	4.069	−179.449	0.000	0.000
LFI24M	4.070	−179.538	4.071	−179.488	0.000	90.000
LFI25S	4.984	61.105	4.981	61.084	−113.200	0.000
LFI25M	4.985	61.065	4.981	61.051	−113.200	89.500
LFI26S	5.037	−61.662	5.040	−61.669	113.200	0.000
LFI26M	5.037	−61.649	5.040	−61.676	113.200	90.500
LFI27S	4.343	153.958	4.343	154.033	−22.300	0.000
LFI27M	4.345	153.981	4.341	154.010	−22.300	89.700
LFI28S	4.374	−153.413	4.376	−153.369	22.300	0.000
LFI28M	4.374	−153.419	4.376	−153.371	22.300	90.300

[a] Beam pointing reconstructed using the first two Jupiter transits (J1 and J2).
[b] Beam pointing reconstructed using the last two Jupiter transits (J3 and J4).
[c] Polarization orientation of the beam measured during ground test.

Table 6. LFI beam FWHM and ellipticity measured in flight from four Jupiter passes.

	FWHM[a] [']	Uncertainty[b] [']	Ellipticity[c]	Uncertainty[b]
70 GHz mean	13.08		1.27	
LFI18 .	13.44	0.03	1.26	0.01
LFI19 .	13.11	0.04	1.27	0.01
LFI20 .	12.84	0.04	1.28	0.01
LFI21 .	12.81	0.03	1.29	0.01
LFI22 .	12.95	0.03	1.28	0.01
LFI23 .	13.33	0.04	1.26	0.01
44 GHz mean	28.09		1.25	
LFI24 .	23.17	0.07	1.37	0.01
LFI25 .	30.60	0.10	1.19	0.01
LFI26 .	30.49	0.12	1.20	0.01
30 GHz mean	33.16		1.37	
LFI27 .	33.09	0.11	1.38	0.01
LFI28 .	33.23	0.11	1.37	0.01

[a] The square root of the product of the major axis and minor axis FWHMs of the individual horn beams, averaged between M and S radiometers.
[b] The standard deviation of the mean of the 1σ statistical uncertainties of the fit. Although a small difference between the M and S beams caused by optics and receiver non-idealities can be expected.
[c] Ratio of the major and minor axes of the fitted elliptical Gaussian.

Collaboration V (2013), two different algorithms were used for calibrating the LFI radiometers in this data release:

1. For the 44 and 70 GHz radiometers, we have used a technique called OSG (optimal search of gain), which is similar to the one used by *WMAP* (Hinshaw et al. 2009). It is based on the fitting of the radiometric signal against the expected dipolar anisotropy induced by the motion of the spacecraft with respect to the CMB rest frame.

2. For the 30 GHz radiometers, we have used a technique that combines the knowledge of the dipolar anisotropy (as above) then additionally takes into account the observed fluctuations in the measurement of the signal of the 4 K reference loads onboard *Planck*.

The overall accuracy in the calibration is reported in Table 1. The reasons why we used two different algorithms are discussed in the Planck Collaboration V (2013). In the following sections we only outline the algorithms.

7.1. Iterative calibration

The iterative calibration algorithm used in the *Planck* LFI can be summarized by the following points:

1. We combine the speed of the spacecraft with respect to the Sun, v_{Planck}, and the speed of the Sun with respect to the CMB, v_{Sun}. To take in account the beam shape we rotate the resulting vector in the beam reference frame using the detector pointings and estimate the direction of the dipole as the dot product between the rotated velocity and previously stored beam parameters. The dipole is then evaluated considering the relativistic correction:

$$\Delta T = T_{CMB} \left(\frac{1}{\gamma(1 - \beta \cos\theta)} - 1 \right), \qquad (5)$$

where $T_{CMB} = 2.7255\,\text{K}$ is the temperature of the CMB monopole and $\cos\theta$ is the direction computed above. We produce discrete time ordered data (TOD) of the expected overall dipole signal for each sample in a pointing period.

Table 7. Mean and standard deviation of FWHM, ellipticity, orientation, and solid angle of the `FEBeCoP` effective beams computed with the `GRASP` beam fitted scanning beams. $\mathrm{FWHM_{eff}}$ is the effective FWHM estimated from the main beam solid angle of the effective beam, $\Omega_{\mathrm{eff}} = \mathrm{mean}(\Omega)$.

Frequency	mean(FWHM)′	σ(FWHM)′	mean(e)	$\sigma(e)$	mean(ψ)°	$\sigma(\psi)$°	mean(Ω) [$arcmin^2$]	$\sigma(\Omega)$ [$arcmin^2$]	$\mathrm{FWHM_{eff}}$
70	13.252	0.033	1.223	0.026	0.587	55.066	200.742	1.027	13.31
44	27.005	0.552	1.034	0.033	0.059	53.767	832.946	31.774	27.12
30	32.239	0.013	1.320	0.031	–0.304	55.349	1189.513	0.842	32.24

2. Using pointing information, we project both V_i and ΔT_i on a `HEALPix` map ($N_{\mathrm{side}} = 256$). Multiple hits on the same pixels are averaged in both cases. The result is a pair of maps, V_k^{map} and $\Delta T_k^{\mathrm{map}}$, with k being the pixel index[2].

3. We use weighted least squares to estimate K in eq. 4 from the correlation between the signal in volts, V_k^{sky}, with $\Delta T_k^{\mathrm{sky}}$:

$$V_k^{\mathrm{map}} = K^{\mathrm{dip}} \Delta T_k^{\mathrm{map}} + \epsilon, \qquad (6)$$

where K and ϵ are the parameters used in the fit. Each sample k is weighted according to the number of hits per pixel. In computing the fit, we use a frequency dependent mask to avoid those pixels where a strong non Gaussian signal other than the dipole is expected, i.e., point sources and the Galaxy.

4. The main source of uncertainties in the fit using the dipole is given by the cosmological (CMB) signal. To improve the result we calibrate the data using K_i and ϵ_i, remove the dipole convolved with the beam and build a map, which represents an estimation of the cosmological signal. To reduce the effect of the noise we combine data streams from both radiometers of the same horn. Then we remove the estimated signal from the data and build a map, apply a simplified destriping algorithm and use the results to correct both K_i and ϵ_i. We iterate the procedure until convergence. The result of this process is a set of gains, K_i^{iter}, and offsets, $\epsilon_i^{\mathrm{iter}}$.

5. An adaptive low-pass filter based on wavelets is applied to the vectors K_i^{iter} and $\epsilon_i^{\mathrm{iter}}$ in order to reduce high-frequency noise, particularly near the regions where the spacecraft is unfavorably aligned with the dipole.

7.2. Calibration using 4K reference load signal

To calibrate the *Planck*/LFI 30 GHz radiometers, we used a different calibration scheme based on the signal measuring the temperature of the 4 K reference loads. This calibration has the advantage of being less dependent on optical systematics such as far sidelobes (Planck Collaboration III 2013), at the expense of being more sensitive to systematics in the radiometers, like ADC non-linearities (Planck Collaboration V 2013). The algorithm can be summarized in the following points:

1. For each pointing period i, a set of gains K_i^{iter} is estimated using the iterative procedure described in section 7.1.

2. The values of K_i^{iter} are used to estimate the value of the constant K_0 in the equation

$$K_i^{\mathrm{iter}} = K_0 \times \left(2 - \frac{V_i^{\mathrm{ref}}}{V^{\mathrm{ref},0}} \right), \qquad (7)$$

where V_i^{ref} is the average value of the 4 K reference load signal (in volts) over the i-th pointing period and $V^{\mathrm{ref}}, 0$ is a voltage representative of the value of V_i^{ref} over the *whole* mission. (We use $V_0^{\mathrm{ref}} = \left\langle V_i^{\mathrm{ref}} \right\rangle$.) The constant K_0 is estimated using a weighted, one-parameter linear least squares fit, where the weights are chosen to be proportional to the expected amplitude of the dipole-like signal in the sky, $\Delta T_i^{\mathrm{dip}}$, at the i-th pointing.

3. Using the value of K_0 estimated in the previous point, we extract a new set of gains $K_i^{4,\mathrm{K}}$ with the equation

$$K_i^{4\,\mathrm{K}} \equiv K_0 \times \left(2 - \frac{V_i^{\mathrm{ref}}}{V^{\mathrm{ref},0}} \right). \qquad (8)$$

The procedure can be modelled by the following GNU R[3] code:

```
data<-data.frame(gain = iterative.dipole.gains,
               vref = 2 - signal.4K/mean(signal.4K),
               dipole = dipole.amplitude.KCMB)
fit<-lm(gain ˜ vref + 0, data, weights = dipole)
gains.4K <- fit$coefficients[1] * data$dvref
```

where `iterative.dipole.gains`, `signal.4K` and `dipole.amplitude.KCMB` are three vectors containing the iterative gains K_i^{iter} before the smoothing filter, the 4 K reference load signal V_i^{ref} averaged over each pointing period, and the values of ΔT_i (eq. 5).

Unlike the procedure in section 7.1, in this case there is no need to smooth the stream of gains, as they share the same stability of the voltages V_i^{ref}.

7.3. Colour Correction

Colour corrections at intermediate spectral indices may be derived accurately from a quadratic fit to the values in Table 8. In addition, the data release includes the `UcCC` IDL package, in common between the two instruments, (Planck Collaboration IX 2013) which calculates colour corrections and unit conversions using the band-averaged bandpass stored in the reduced instrument model (RIMO) file also included in the data release. The way this table has been computed is fully described in Planck Collaboration V (2013).

8. Noise estimation

The estimation of noise properties is fundamental in several aspects of the *Planck* LFI data analysis. For instance, such measurements are used in the Monte Carlo simulations of noise necessary for power spectra estimations, as well as to determine

---

[2] Most of the pixels in the maps are not set, as during one pointing period the beam paints a thin circle in the sky. We assume hereafter that the index k runs only through the pixels which have been hit at least once.

[3] http://www.r-project.org/.

Table 8. Multiplicative colour corrections cc(α) for individual LFI Radiometer Chain Assemblies and for the band average maps.

Horn	Spectral index α												
	−2.0	−1.5	−1.0	−0.5	0.0	0.5	1.0	1.5	2.0	2.5	3.0	3.5	4.0
LFI-18	0.948	0.961	0.972	0.981	0.988	0.994	0.997	0.998	0.997	0.995	0.990	0.983	0.975
LFI-19	0.856	0.878	0.899	0.919	0.939	0.957	0.975	0.991	1.006	1.020	1.032	1.043	1.053
LFI-20	0.889	0.908	0.925	0.941	0.956	0.970	0.983	0.994	1.003	1.011	1.018	1.023	1.027
LFI-21	0.917	0.933	0.947	0.960	0.971	0.981	0.989	0.996	1.001	1.004	1.006	1.006	1.004
LFI-22	1.024	1.026	1.027	1.026	1.023	1.018	1.011	1.003	0.993	0.982	0.969	0.955	0.940
LFI-23	0.985	0.991	0.996	0.999	1.001	1.002	1.002	1.000	0.997	0.993	0.988	0.982	0.975
70 GHz	0.938	0.951	0.963	0.973	0.982	0.988	0.994	0.997	0.999	0.999	0.998	0.995	0.991
LFI-24	0.978	0.984	0.988	0.993	0.996	0.998	0.999	1.000	0.999	0.998	0.996	0.993	0.989
LFI-25	0.967	0.974	0.980	0.985	0.990	0.994	0.996	0.999	1.000	1.000	1.000	0.999	0.997
LFI-26	0.957	0.966	0.973	0.980	0.985	0.990	0.995	0.998	1.000	1.001	1.002	1.002	1.000
44 GHz	0.968	0.975	0.981	0.986	0.990	0.994	0.997	0.999	1.000	1.000	0.999	0.998	0.995
LFI-27	0.948	0.959	0.969	0.978	0.985	0.991	0.995	0.998	1.000	1.000	0.998	0.995	0.991
LFI-28	0.946	0.958	0.968	0.977	0.985	0.991	0.996	0.998	1.000	0.999	0.997	0.993	0.988
30 GHz	0.947	0.959	0.969	0.977	0.985	0.991	0.995	0.998	1.000	1.000	0.998	0.994	0.989

proper horn weights to be employed during the map-making process. In addition, inspection of noise properties during mission life time is of paramount importance in tracking possible variations and anomalies in instrument behaviour/performance. In this respect we have improved our noise estimation pipeline compared to that used in Zacchei et al. (2011), implementing a Monte Carlo Markov Chain approach for the extraction of basic noise parameters such as the white noise level, knee-frequency and slope of the $1/f$ noise at low frequencies. This allows for an un-biased estimation of the last two noise parameters compared to the previously implemented log-periodogram approach (Zacchei et al. 2011).

The code works as follows. It assumes a functional form for noise spectrum:

$$P(f) = \sigma^2 \left[1 + \left(\frac{f}{f_k} \right)^{\beta} \right], \qquad (9)$$

with three basic parameters. It is also possible to work with a functional form with two more parameters:

$$P(f) = \sigma^2 \left[1 + \left(\frac{f}{f_{k1}} \right)^{\beta_1} + \left(\frac{f}{f_{k2}} \right)^{\beta_2} \right]. \qquad (10)$$

The latter could be useful when there are clearly two different behaviour in the low-frequency part of the spectrum where, beside usual radiometric $1/f$ noise, the signature of noise induced by thermal fluctuations appears.

As for the white noise part, this is, as before, computed making a simple average of noise spectrum on the last 10% of frequency bins (the high-frequency tail of the noise spectrum). This percentage works well for almost all radiometers at 44 and 70 GHz but is quite delicate for the 30 GHz radiometers which show typical values of knee-frequency around 100 mHz, and therefore require a smaller percentage to get an un-biased white noise estimation. Once white noise is computed, the code creates Markov Chains for the other parameters. Discarding the burn-in period of the chains we can directly get the expected value and variance of each noise parameter sampled from the chain distribution.

The upper panel of Fig. 4 shows a typical spectrum at 70 GHz with the simple log-periodogram fit (red line) and the new MCMC derived spectrum (blue line) superimposed. The right panel instead shows the distribution for knee-frequency and slope derived from the example spectrum.

8.1. Updated noise properties

Radiometer noise properties have been evaluated with the new code implementing the Monte Carlo Markov Chain approach described in the section above. As for the previous release of LFI data, we select radiometer calibrated data in chunks of five ODs and compute noise spectra with the roma iterative generalized least square (IGLS) map-making algorithm (Natoli et al. 2001; de Gasperis et al. 2005), which includes a noise estimation tool based on the iterative approach described in Prunet et al. (2001). The actual algorithm is described therein and the interested reader can find its application to LFI data in Zacchei et al. (2011). The output is a frequency spectrum on which the new MCMC code is applied. Results at radiometer level on white noise sensitivity are reported in Table 9, while Table 10 shows $1/f$ noise parameters. These are computed taking the median of the five estimations made for different ranges of OD over the nominal mission time.

As a matter of fact, time variations of the noise properties provide a valuable diagnostic of possible changes of instrument behavior. We know that there was quite a dramatic change in LFI operations, namely the switch over between the two sorption coolers. We expect to see variations in the noise properties during the degradation process of the first cooler and at the onset of the redundant one.

Figure 5 shows a set of noise frequency spectra for three LFI radiometers (LFI28M, LFI24S and LFI18M) based on the period considered for the 2013 data release. Some comments are in order. First of all, the white noise level is extremely stable in all three cases shown; this is also true for all the LFI radiometers. Also the knee-frequency and slopes are quite stable, as clearly demonstrated by the noise spectra until OD 326. After that time the spectra show an increasing noise and two slopes for the low-frequency part. The latter becomes more evident for spectra around OD 366 and OD 466, when the first cooler starts to be less effective and produces low-frequency thermal noise. This behavior is present at some level in all radiometers, but with different trends, ranging from the small effect shown by LFI24S to more prominent effects as shown by LFI28M and LFI18M.
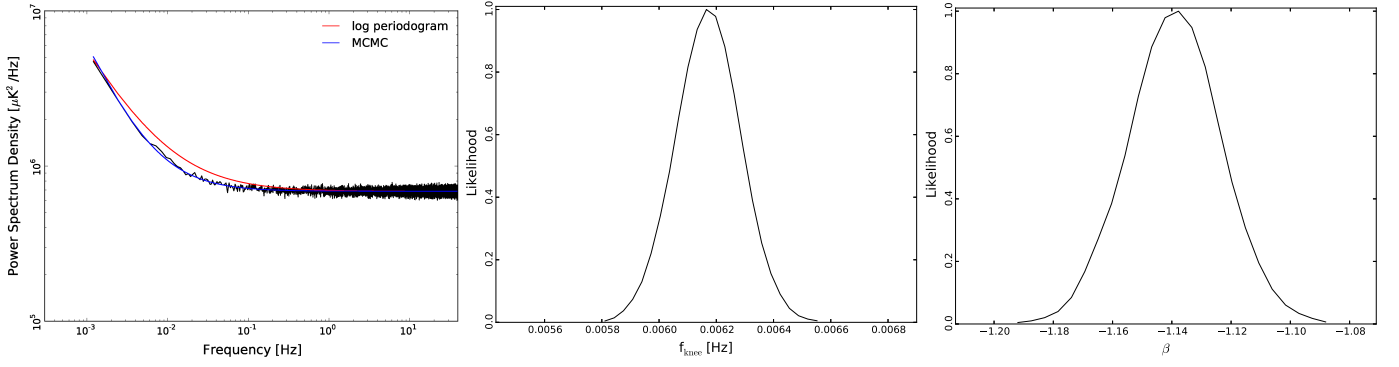
Fig. 4. *Left*: typical noise spectrum at 70 GHz with simple log-periodogram fit (red line) and the new MCMC fit (blue line). *Centre*: sample distrubution for the knee-frequency and slope (*Right*) for the example spectrum.
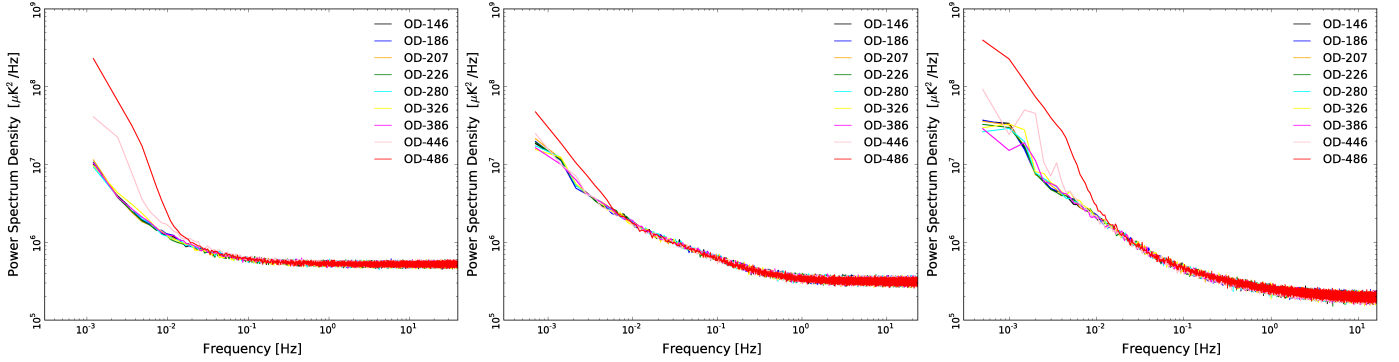

Fig. 5. Time behavior of noise spectra for three LFI radiometers (*Left* LFI 18M 70 GHz, *Centre* LFI 24S 44 GHz and *Right* LFI 28m 30 GHz). In all cases white noise is extremely stable as is the $1/f$ noise until OD 326. After that period, the degradation of the sorption cooler and the switch-over to the redundant cooler introduce higher thermal noise at the lowest frequencies.

Table 9. White noise sensitivities for the LFI radiometers.

	White Noise Sensitivity	
	Radiometer M $[\mu K_{CMB} s^{1/2}]$	Radiometer S $[\mu K_{CMB} s^{1/2}]$
70 GHz		
LFI18	511.7 ±1.7	466.3 ±1.7
LFI19	579.8 ±1.6	554.1 ±1.6
LFI20	587.5 ±1.4	619.7 ±2.1
LFI21	451.6 ±1.7	560.9 ±1.7
LFI22	489.9 ±1.5	531.0 ±2.1
LFI23	503.4 ±1.8	538.8 ±1.9
44 GHz		
LFI24	461.0 ±1.3	398.2 ±1.3
LFI25	413.5 ±1.5	393.3 ±3.0
LFI26	480.8 ±1.5	419.1 ±1.9
30 GHz		
LFI27	282.2 ±2.1	304.7 ±2.0
LFI28	318.2 ±1.9	286.8 ±2.1

9. Map-Making

The mapmaking pipeline was already described in detail in the Zacchei et al. (2011) and other papers. Here we will only describe the overall process reporting significant updates. Subsections will be dedicated to special processes such as the calculation of the noise covariance matrices, half-ring maps,

survey-maps and Monte Carlo maps simulations used in the validation process.

9.1. `MADAM` *pipeline for frequency maps*

LFI frequency maps were produced by the `Madam` mapmaking code (Keihänen et al. 2010). The code takes as input the calibrated TOD for each radiometer, and the corresponding radiometer pointing data, in the form of three Euler angles (θ, ϕ, ψ). The primary output consists of three pixelized Stokes maps *(T,Q,U)*, which represent the temperature and polarization anisotropies of the observed sky.

The algorithm is based on the destriping technique, where the correlated noise component is modelled by a sequence of offsets, or baselines. The amplitudes of these baselines are determined through maximum-likelihood analysis. Higher-frequency noise, which is not captured by the baseline model, is assumed to be purely white.

The noise model can be written as

$$n' = Fa + n \qquad (11)$$

Here n' is the total noise stream, n represents white noise, a is a vector consisting of the baselines, and F is a matrix, consisting of ones and zeros, which spreads the baselines into a time-ordered data stream.

Unlike conventional destriping, `Madam` also uses information on the known noise properties, in the form of a noise prior. This allows one to extend the destriping approach to very short baseline lengths, well below the scanning period of a minute.

Table 10. Knee frequency and slope (power of frequency) for the LFI radiometers.

	KNEE FREQUENCY		SLOPE	
	Radiometer M [mHz]	Radiometer S [mHz]	Radiometer M	Radiometer S
70 GHz				
LFI18	15.3 ±2.8	18.3 ±1.6	−1.07 ±0.11	−1.20 ±0.15
LFI19	11.9 ±1.3	14.6 ±1.1	−1.22 ±0.30	−1.12 ±0.16
LFI20	8.4 ±1.9	6.0 ±1.7	−1.31 ±0.40	−1.34 ±0.47
LFI21	39.3 ±4.0	14.0 ±2.4	−1.26 ±0.09	−1.24 ±0.11
LFI22	10.1 ±2.1	15.9 ±7.1	−1.53 ±0.34	−1.20 ±0.36
LFI23	30.2 ±1.4	58.8 ±9.0	−1.07 ±0.03	−1.21 ±0.05
44 GHz				
LFI24	26.9 ±1.2	73.0 ±7.9	−0.94 ±0.01	−0.91 ±0.01
LFI25	20.1 ±0.6	46.1 ±1.8	−0.85 ±0.01	−0.90 ±0.01
LFI26	64.4 ±2.0	43.8 ±8.9	−0.92 ±0.01	−0.88 ±0.06
30 GHz				
LFI27	175.1 ±2.2	109.6 ±2.3	−0.93 ±0.01	−0.91 ±0.01
LFI28	127.9 ±3.8	43.9 ±2.2	−0.93 ±0.01	−0.91 ±0.02

The baseline length is a key parameter in the destriping technique. We chose the baseline length so that it corresponds roughly to one second of sampling time, while also requiring it to be an integral number of samples. The chosen baseline lengths were 33, 47, and 79 samples, for the 30, 44, and 70 GHz channels, respectively. These correspond to 1.0151, 1.0098, and 1.0029 s, respectively.

The baseline length of one second is a reasonable compromise between computational burden and the quality of the final map. Shortening the baseline further, below one second, has very little effect on the residual noise.

When mapmaking is run with a short baseline, the noise prior plays an important role. There are not enough crossing points between the one-second data sections to determine the baselines without inserting additional a priori information to constrain the solution. In this case, the required additional information is the noise prior, which was constructed from the parametrized noise model (knee frequency, slope, white noise variance), based on the parameters given in Tables 9 and 10. From these we compute the expected covariance between the noise baselines, $C_a = \langle aa^T \rangle$. The exact derivation is given in Keihänen et al. (2010). Another important role of the noise prior is to suppress the signal error, which would otherwise increase rapidly with decreasing baseline length. Flagged data sections were handled by setting the white noise variance formally to infinity for those samples, but not altering the baseline pattern. The flagged samples thus do not contribute to the final map in any other way than serving as space-holders which keep the correct distance between unflagged samples on both sides of the gap. This is essential for the noise prior to be applied correctly.

The use of a priori information has the danger of hiding problems in the data, since the prior may drive the solution to a correct-looking result, even if the data alone were not in complete agreement with it. To avoid this pitfall, we computed for comparison a subset of the maps with a one-minute baseline, without using a noise prior, and compared the maps visually. No artifacts could be seen in either of the maps. Despite the triviality of the check, similar sanity checks helped to reveal bugs at earlier stages of the development of the data processing pipeline.

`Madam` uses `HEALPix` pixelisation to discretize the sky. Each data sample is assigned as a whole into the pixel where the center of the beam falls. We used resolution $N_{side} = 1024$ for all LFI frequencies. The average width of one pixel at this resolution is 3.5′. The chosen resolution gives complete sky coverage for the 70 GHz channel. At 30 GHz and 44 GHz, where the sampling frequency is lower, there remain individual unobserved pixels, which are marked by a special value in the product maps. In the 30 GHz frequency map there are 158 and and in the 44 GHz frequency map 250 missing pixels (0.0013% and 0.0020%, respectively). These count also the pixels which were covered with insufficient polarisation angle coverage, and for which we could not recover the polarisation component. The pixel size is to be compared with the beam resolution at each frequency (Table 3).

The maximum-likelihood analysis, which lies behind our mapmaking algorithm, and derivation of the destriping solution, are presented in Keihänen et al. (2010). Here we quote the most important formulas for easier reference.

The vector of baseline a is solved from the linear equation

$$(F^T C_w^{-1} Z F + C_a^{-1})a = F^T C_w^{-1} Z y, \tag{12}$$

where

$$Z = I - (P^T C_w^{-1} P)^{-1} P^T C_w^{-1}. \tag{13}$$

The final map is then constructed as

$$m = (P^T C_w^{-1} P)^{-1} P^T C_w^{-1} (y - Fa), \tag{14}$$

where a is the baseline solution. Here F is a matrix, consisting of ones and zeros, which spreads the baselines into time-ordered data. P is the pointing matrix, which picks values from the T, Q, U maps and spreads them into time-ordered data, and y is the observed data stream. The covariance matrices C_a and C_w represent the a priori known properties of the baselines and the white noise component, respectively. The white noise component is assumed to be uncorrelated, but not necessarily with uniform variance. Matrix C_w is thus diagonal, but not constant.

Matrices P, F, C_w are very large, but sparse. They are not constructed explicitly, but the operations represented formally as matrix multiplication above, are performed algorithmically. For instance, multiplication by P^T represents an operation where the time-ordered data are coadded on a sky map.

We solve Eq. 12 through conjugate gradient iteration. Convergence was reached typically after 20−100 iterations, depending on the sky coverage and radiometer combination. Full

mission maps, where the whole sky was covered, typically converge faster than single-survey maps.

The observed signal can be written as

$$y_i = T(\omega_i) + Q(\omega_i) \cos(2\psi_i) + U(\omega_i) \sin(2\psi_i), \qquad (15)$$

where ω_i is the sky pixel where the sample is assigned to, and ψ_i defines the beam orientation. The elements of the pointing matrix P consist of ones and cosine and sine factors picked from this equation.

When constructing single-horn maps, we included only the temperature component of the sky into the computation. In the case of frequency or horn-pair maps we included three map components, corresponding to the I,Q,U Stokes components, although only the I component maps are included in the 2013 data release.

We deviate from the formulation of the original `Madam` paper in that we have written C_w in place of C_n. This reflects the fact that the C_w matrix we insert into the solution is not necessarily the white noise covariance, but rather a user-defined weighting factor. We decided to diverge from the exact maximum-likelihood solution in order to have better control over systematics. The weight was constructed according to a horn-uniform weighting scheme, as follows. The weight for a given horn was chosen to be

$$C_w^{-1} = \frac{2}{\sigma_M^2 + \sigma_S^2} \qquad (16)$$

where σ_M and σ_S are the white noise sensitivities of the two radiometers of the horn, computed from the values given in Table 3. The weights were identical for radiometers of same horn. The formula above is applied for non-flagged samples. For flagged samples we set $C_w^{-1} = 0$.

When horn-uniform weighting is applied, the polarization maps become dependent solely on the signal difference between M and S radiometers, apart from a small leakage due to the fact the polarization sensitivities are not exactly at 90° from each other. Many systematic effects, which are equal or strongly correlated within a horn, cancel out in the differentiation. In particular, the horn-uniform weighting has the benefit of reducing spurious polarization signals arising from beam shape mismatch, since the beam shapes of a radiometer pair sharing a horn are typically quite similar (though not identical). Complete cancellation also requires that the same flags are applied to both data streams. Therefore, if a sample for one radiometer was flagged, we discarded the corresponding sample for the other radiometer as well.

The covariance of residual white noise in the map solution is obtained from

$$C_{\mathrm{wn}} = (P^{\mathrm{T}}C_w^{-1}P)^{-1}P^{\mathrm{T}}C_w^{-1}C_nC_w^{-1}P(P^{\mathrm{T}}C_w^{-1}P)^{-1} \qquad (17)$$

where now C_n is the actual white noise covariance of the time-ordered data. For a given C_n, the residual noise is minimized when $C_w = C_n$, in which case $C_{\mathrm{wn}} = (P^{\mathrm{T}}C_n^{-1}P)^{-1}$. In using a different weighting we thus sacrifice some noise sensitivity for better removal of systematics.

Note that altering matrix C_w does not introduce bias into the solution, as may easily be verified by inserting $y = Pm$ in the solution above. It merely affects the level of residual noise.

The white noise covariance only takes into account the uncorrelated component of the noise. The computation of a full noise covariance matrix, which also captures the residual correlated noise, is discussed in a separate section below.

The destriping solution assumes that the sky signal is uniform within one pixel. This is not strictly true, which gives rise

to the signal error: signal differences within a pixel are falsely interpreted as noise, which leads to spurious striping, especially in the vicinity of point sources or in other regions where the signal gradient is large. Most of the effect comes from the Galactic region.

Similarly, mismatch in frequency response between radiometers gives rise to spurious striping, as different radiometers record slightly different signals from the same source. In this case also the main effect comes from the Galactic region, where foreground emission is strong.

To reduce these undesired effects, we masked out the Galactic region and point sources in the destriping process. We used crossing points of rings only outside the masked region to solve the noise baselines, though all the data was included in the construction of the final map product. The masks for 30, 44, and 70 GHz left uncovered 78.7%, 89.4%, and 89.7% of the sky, respectively (fraction of sky included in the analysis). Some of the baselines fall completely inside the masked region, but can still be recovered with reasonable accuracy with help of combined information of the neighbouring baselines and the noise prior.

In Table 11 we list the delivered maps. All the maps have `HEALPix` resolution $N_{\mathrm{side}} = 1024$.

9.2. Low Resolution data set

To fully exploit the information contained in the large scale structure of the microwave sky, pixel-pixel covariances are needed in the maximum likelihood estimation of the CMB power spectrum. However, full covariance matrices are impossible to employ at the native map resolution, because of resource limitations. A low-resolution dataset is therefore required for the low-ℓ analysis. This dataset consists of low-resolution maps, and descriptions of residual noise present in those maps given by pixel-pixel noise covariance matrices (NCVMs).

The low-resolution dataset can currently be utilized efficiently only at resolution $N_{\mathrm{side}} = 16$, or lower. All the low-resolution data products are produced at this target resolution.

We will first discuss the production of the low-resolution maps, and then continue the discussion on the NCVMs.

9.2.1. Low-resolution maps

Different schemes to produce the low-resolution maps are discussed in Keskitalo et al. (2010). We chose to construct low-resolution maps by downgrading the high-resolution maps to the target resolution, $N_{\mathrm{side}} = 16$, using a noise-weighted downgrading scheme. A low-resolution map was obtained by applying to its high-resolution counterpart the operation

$$m_{\mathrm{l}} = (P_{\mathrm{l}}^{\mathrm{T}}C_w^{-1}P_{\mathrm{l}})^{-1}X(P_{\mathrm{h}}^{\mathrm{T}}C_w^{-1}P_{\mathrm{h}})m_{\mathrm{h}} \equiv Dm_{\mathrm{h}},$$

where X_{qp} sums the high-resolution pixels to the low-resolution,

$$X_{qp} = \begin{cases} 1, & p \text{ subpixel of } q \\ 0, & \text{otherwise.} \end{cases}$$

Here subscripts h, l refer to the high ($N_{\mathrm{side}} = 1024$) and low ($N_{\mathrm{side}} = 16$) resolution versions of the pointing matrix. The same matrix X downgrades the pointing matrix, $P_{\mathrm{l}} = P_{\mathrm{h}}X^{\mathrm{T}}$. The resulting map is identical to the one we would get by solving the baselines at the higher resolution, but then binning the map to a lower resolution.

By using the noise-weighted downgrading scheme, we get an adequate control over signal and noise in the resulting map.

Table 11. Released LFI maps.

Map	Horns	OD range	Baseline (s)	Sky coverage (%)
30 GHz nominal	27, 28	91-563	1.0151	99.999
30 GHz survey 1	27, 28	91-270	1.0151	97.205
30 GHz survey 2	27, 28	270-456	1.0151	97.484
44 GHz nominal	24, 25, 26	91-563	1.0098	99.998
44 GHz survey 1	24, 25, 26	91-270	1.0098	93.934
44 GHz survey 2	24, 25, 26	270-456	1.0098	93.310
70 GHz nominal	18, 19, 20, 21, 22, 23	91-563	1.0029	100.000
70 GHz survey 1	18, 19, 20, 21, 22, 23	91-270	1.0029	97.938
70 GHz survey 2	18, 19, 20, 21, 22, 23	270-456	1.0029	97.474

If we were to calculate a low-resolution map directly at the target resolution, the signal error would be larger due to sub pixel structures, while the noise level would be lower.

After downgrading, the temperature component was smoothed with a symmetric Gaussian window function with FWHM = 440′, while the polarization components were left unsmoothed. Smoothing was applied to alleviate aliasing due to high frequency power in the map. The polarization components need to be treated differently, since the cosmological information contained in polarization has several orders of magnitude poorer signal-to-noise ratio. Compared to the approach proposed in Keskitalo et al. (2010), we intentionally changed the order of downgrading and smoothing to better deal with noise. The aliased power is negligible at scales unaffected by the smoothing operator.

9.2.2. Noise covariance matrices

The statistical description of the residual noise present in a low-resolution map is given in the form of a pixel-pixel noise covariance matrix, as described in Keskitalo et al. (2010). We must apply the processing steps chosen in the map downgrading to NCVMs for consistency. Some approximations were however required: some are inherent to the `Madam` map-maker NCVM module, while some were made due to performance issues.

The pixel-pixel noise covariance matrix for generalized destriping is

$$N = (P^{\mathrm{T}}(C_w + FC_aF^{\mathrm{T}})^{-1}P)^{-1},$$

which can be written in a dimensionally reduced form as

$$N^{-1} = P^{\mathrm{T}}C_w^{-1}P - P^{\mathrm{T}}C_w^{-1}F(F^{\mathrm{T}}C_w^{-1}F + C_a^{-1})^{-1}F^{\mathrm{T}}C_w^{-1}P \quad (18)$$

Applying Eq. 18 in practice, lead to the need of inverting a symmetric $3N_{\mathrm{pix}} \times 3N_{\mathrm{pix}}$ matrix in a later analysis step. Because the inverse NCVMs are additive, we divided the computations into a number of small chunks to save computational resources. We first calculated, using Eq. 18 one inverse NCVM per radiometer per survey at the highest possible resolution $N_{\mathrm{side}} = 32$ permitted by computer resources. Later we combined the individual inverse matrices to the actual inverse matrices.

To obtain the noise covariance from its inverse, the matrices were inverted using the eigendecomposition of a matrix. The monopole of the temperature map cannot be resolved by the map-maker, and thus the matrix becomes singular. Therefore the ill-determined mode was left out of the analysis.

These intermediate resolution matrices are then downgraded to the target resolution. The downgrading operator is the same D as for the map downgrading, but P_{h} is replaced with P_{i}, i.e., with the intermediate resolution pointing matrix. The downgraded matrix is

$$N_l = DND^{\mathrm{T}}. \quad (19)$$

As a final step the same smoothing operator was applied to the temperature component of the matrices as was applied to the low-resolution maps.

The noise covariance matrices were calculated with two different sets of noise parameters. One set covered the entire mission under consideration (values given in Tables 9 and 10), while the other had individual noise parameters for each survey.

Equation 18 describes the noise correlations in a situation where the noise baselines are solved at the resolution of the final map. For an exact description of the correlations, we should construct the matrix at resolution $N_{\mathrm{side}} = 1024$, and downgrade the inverted matrix to the target resolution $N_{\mathrm{side}} = 16$. This is not feasible, due to the size of the matrix. We therefore construct the matrix at the highest possible resolution $N_{\mathrm{side}} = 32$, and downgrade it to the target resolution.

The same formula inherently assumes that individual detectors are weighted according to their white noise levels, as suggested by maximum likelihood analysis. In map-making, however, we apply horn-uniform weighting, to have better control over systematics, as explained in the previous section. Also, the formulation does not take into account the effect of the destriping mask. As results of these idealizations, the covariance matrix is an approximate description of the residual noise correlations. We have performed χ^2 tests to assess the effect of each idealization individually.

Figure 6 illustrates the effect of removing the approximations inherent in the NCVM computation: no horn-uniform weighting; the destriping resolution, $N_{\mathrm{Destr.}}$, equalling the map resolution; and no masking in the destriping phase. Each non-ideal factor increases the discrepancy seen in the χ^2 test.

We chose to use shorter baselines in the NCVM production than in the map-making. They were 0.25 s / 8 samples, 0.5 s / 24 samples, and 0.5 s / 39 samples for 30 GHz, 44 GHz and 70 GHz, respectively. Since the knee frequencies were higher than anticipated prior to launch, short baselines model the noise better (Keskitalo et al. 2010). We additionally found out that reducing baseline length in the NCVM calculation affects the χ^2 statistics more than changing baseline length in the map-making (see Fig. 7).

9.3. Half ring noise maps

In order to estimate the noise directly at the map level and in the angular power spectra, we produced half-ring maps (h_1 and h_2) with the same pipeline as described in Sect. 9.1, but using data only from the first or the second half of each stable pointing period. These half-ring maps contain the same sky signal,
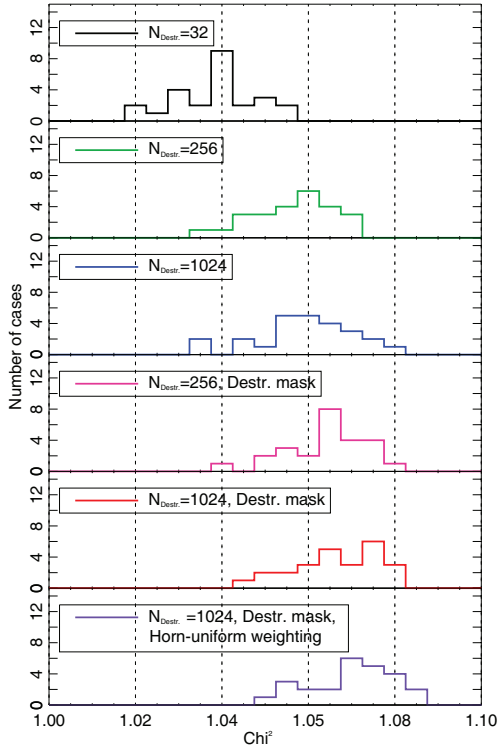
Fig. 6. Reduced χ^2 statistics from 25 noise only maps for 30 GHz 2013 delivery. The NCVM was calculated using 0.25 s baselines, while the simulations were made with 0.5 s baselines. The number of idealizations in the noise only simulations decreases from top to bottom. The first set of simulations (plotted in black) contains the same approximations that are made in the NCVM calculation. The last set of simulations (plotted in purple) corresponds to the standard map-making options: the horns are weighted uniformly; destriping resolution, $N_{\mathrm{Destr.}}$, is 1024; and a destriping mask is applied.

since they result from the same scanning pattern on the sky. Therefore the difference of maps h_1 and h_2 captures any noise that varies faster than half of the duration of the pointing period, i.e., the noise whose frequency is $f \gtrsim 1/20 \, \mathrm{min} = 0.85 \, \mathrm{mHz}$. The procedure of calculating the half-ring maps and their hit count weighted difference maps is described in more detail by Zacchei et al. (2011) and Planck Collaboration ES (2013).

The use of half-ring maps in the validation of data and noise estimates will be explained in Sect. 12. In addition, the half-ring maps were an integral part of the component separation process Planck Collaboration XII (2013) and likelihood codes Planck Collaboration XV (2013).

9.4. Noise Monte Carlo simulations

Simulated noise timelines were produced according to the three-parameter noise model (white noise sensitivity, knee frequency, slope), using the estimated values for these parameters given in Tables 9 and 10. Maps were made from this simulated noise using reconstructed flight pointing and the same `Madam` parameter settings as were used for the flight maps. These steps were repeated to produce a Monte Carlo set of 1000 realizations of noise maps for different radiometer combinations, including frequency maps and 70 GHz horn-pair maps.

For LFI, this Monte Carlo (MC) work was done in two stages, with two partially different pipelines, first an LFI MC
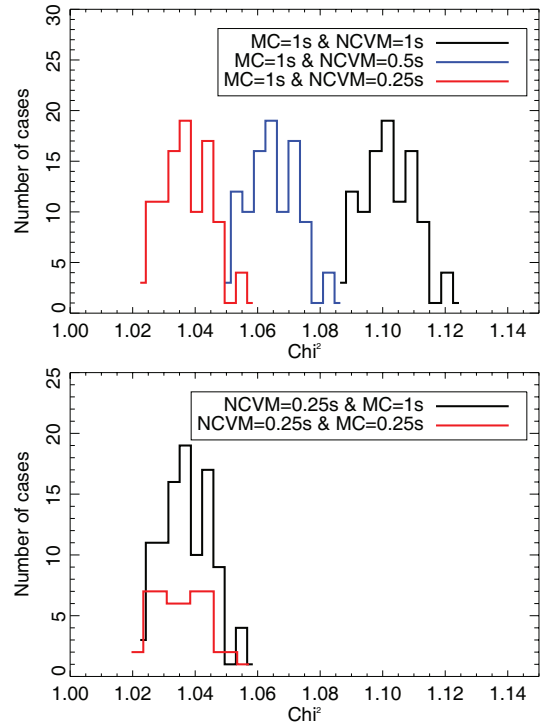
Fig. 7. The reduced χ^2 statistics from noise only maps for 30 GHz 2013 delivery. *Upper*: the noise only simulation set is fixed, while the NCVM baseline length changes. The baseline lengths in the NCVM calculation were 1 s, 0.5 s, and 0.25 s, and are plotted in black, blue, and red respectively. *Lower*: the NCVM is fixed, while the noise only simulation varies. Two baseline lengths were chosen 1 s (plotted in black) and 0.25 s (red).

in close connection with the map-making from the LFI flight data, and then as a part of the joint LFI/HFI full-focal plane "FFP6" simulations. This work was divided between two supercomputing centers, CSC–IT Center for Science in Finland and the National Energy Research Scientific Computing Center (NERSC) in U.S.

The noise MC maps provide a statistical distribution of noise maps that can be compared to the half-ring noise maps (Sec. 9.3), to see how well maps from the noise model match the real flight noise in the half-ring noise maps. We note, however, that the half-ring noise maps do not represent properly the noise in the flight maps for the lowest frequencies, i.e., for time scales of the order of half the pointing period or longer.

For low-resolution studies the maps were downgraded to $N_{\mathrm{side}} = 32$ and $N_{\mathrm{side}} = 16$ `HEALPix` resolution, using the same procedure as for the flight maps. These can be compared to the low-resolution noise covariance matrices discussed in Sec. 9.2, which were generated from the same noise model, but are based on some approximations. Thus this comparison, see Fig. 6 and Fig. 7, shows the effect of these approximations on the NCVM.

In addition the noise MC maps were used in power spectrum estimation, component separation (Planck Collaboration XII 2013), and in non-Gaussianity estimation (Planck Collaboration XXIII 2013) and (Planck Collaboration XXIII 2013).

9.5. Overview of LFI map properties

Figures 8 to 10 show the sky frequency maps created from LFI data. The top row of each figure shows the temperature maps

based on the nominal mission data, while the second row shows the differences between maps, n_m, made of the first and second half of each stable pointing period (half-ring maps) weighted by the hit count calculated from equation 21. These maps provide an intuitive evidence of the level and distribution of the residuals and are calculated as

$$n_m = \frac{h_1 - h_2}{w_{hit}}, \qquad (20)$$

where the hit count weight is

$$w_{hit} = \sqrt{hit_{full} \left[\frac{1}{hit_1} + \frac{1}{hit_2} \right]}. \qquad (21)$$

Here $hit_{full} = hit_1 + hit_2$ is the hit count of the full map m, while hit_1 and hit_2 are the hit counts of the haf-ring maps h_1 and h_2, respectively.

The third row shows the difference in the sky between the first and second survey, and gives information on longer time scale variations. In the half-ring difference maps a darker stripe, corresponding to two observation days, is visible due to higher noise (it is barely visible also in the frequency maps). This is due to the fact that in the first days of observation the LFI instrument was affected by an occasional bit-flip change in the gain-setting circuit of the data acquisition electronics, probably due to cosmic ray hits; at that time we did not know the cause of the problem and we were obliged to perform some operations to identify and solve it. The data acquired during this period, and contributing to the visible ring, have been flagged out. One other clear feature can be seen on the Galactic plane in the survey difference maps, especially at 30 GHz. This apparent split in intensity is due to the beam ellipticity: the elliptical beam had a different orientation relative to the Galaxy in the first survey compared with the second.

10. Polarization

The LFI data processing has included analysis of polarization from the beginning, but polarization results are not included in the current data release and scientific analysis, because the level of systematic errors in the maps remains above acceptable levels. In this section we briefly outline the polarization-specific steps in the data analysis, quantify the residual systematics, and sketch how we expect to correct them for the next data release.

To an excellent approximation (see Sect. 9.1) the LFI polarization maps (Stokes parameters Q and U) are derived from the difference between the calibrated signals from the two radiometers in each RCA, so-called main-arm (M) and side-arm (S), which are sensitive to orthogonal polarizations. Any differential calibration errors between M and S cause leakage of total intensity into the polarization maps. Such mismatch arises from three main causes:

– differences between the beam profiles of M and S;
– errors in the gain calibration;
– differential colour corrections between M and S due to differences in their bandpasses (the 'bandpass leakage') effect.

All these effects are described in Leahy et al. (2010). Only the bandpass leakage requires a special step in the calibration, although polarization imposes stringent requirements on the accuracy of gain calibration which have driven our choice of calibration scheme (Planck Collaboration V 2013). The control of systematics for polarization also require precise cancellation of the

M and S arm signals, which underlies our choice to use identical pointings for the data from the two radiometers in each horn, despite a small amount of beam squint between the polarizations, and also the decision to use horn-uniform weighting. Neither of these choices results in significant degradation to the total intensity maps although they are slightly non-optimal.

The principle instrumental factor controlling bandpass leakage is the effective frequency mismatch between M and S detectors, $a = (\nu_S - \nu_M)/2\nu_0$, which must be combined with estimates of the "leakage amplitude" of the foreground emission, $L = (\beta_{fg} - \beta_{CMB})T_{fg}$. Because the leakage amplitude relies on products from component separation, maps of L are available at no higher resolution than that of the 30 GHz channel (33.16 ′), and are most reliable at lower resolution (1°), where our analysis can incorporate the *WMAP* 22 GHz maps.

In principle the a-factors can be estimated from the bandpass profiles measured in the ground calibration campaign (Zonca et al. 2009), but as anticipated by Leahy et al. (2010), more accurate values can be found from the flight data; a detailed description of our approach to this will be discussed in a future paper. We estimate that our a-factors are currently accurate to about 0.05%, based on the scatter in values derived from different calibrators. A bigger problem at present is accurate evaluation of the leakage amplitude, which requires not only excellent separation of CMB and foreground emission but also accurate estimates of the foreground spectral index within the band. Currently, the combined uncertainty in the bandpass leakage correction is about 0.3% of the local foreground intensity. This is comparable to the mean polarization fraction along the Galactic plane.

One other parameter in principle should be calibrated for polarization: the precise orientation of the polarization response for each feed horn. As noted by Leahy et al. (2010), knowledge of horn orientation was expected to be good to better than 1° from the construction tolerances, even though it was not possible to calibrate them directly. In flight, we check these values by observations of the Crab nebula, and the results confirm the orientations to within a few degrees, which is sufficient for analysis of the E-mode spectra. At a higher level of precision our estimates of the response orientations are still affected by the uncertainty in a-factors, and so as yet we have no evidence to reject the nominal orientation angles.

The most interesting cosmological signal visible in LFI polarization is the very large-scale ($\ell < 10$) E-mode peak due to reionisation, at a typical brightness level of $0.3\,\mu K$. Crucial tests of the reliability of this signal are that the B-mode and EB cross-correlation spectra should contain negligible signal, since a cosmological B-mode signal at this level would correspond to a tensor-to-scalar ratio significantly larger than current upper limits, while the cosmological EB mode is precisely zero. The primary channel for cosmology is 70 GHz, which has the least foreground contamination of all *Planck* channels; our likelihood pipeline estimates these spectra using a conservative Galactic mask and corrects for residual foregrounds based on *Planck* 30 GHz map and/or *WMAP* maps. With our current calibration, both these spectra contain residuals at a level comparable to the expected E-mode signal from reionisation. Hence, although the latter is apparently detected, we cannot be confident that the signal is real. This situation is better illustrated in Fig. 12 where we report, at all three LFI frequencies, null tests spectra from survey-survey differences. A comment is in order here. At all frequencies the null test EE spectra are in very good agreement with the expected noise level as traced by half-ring difference maps at multipoles larger of few tens: this is an indi-
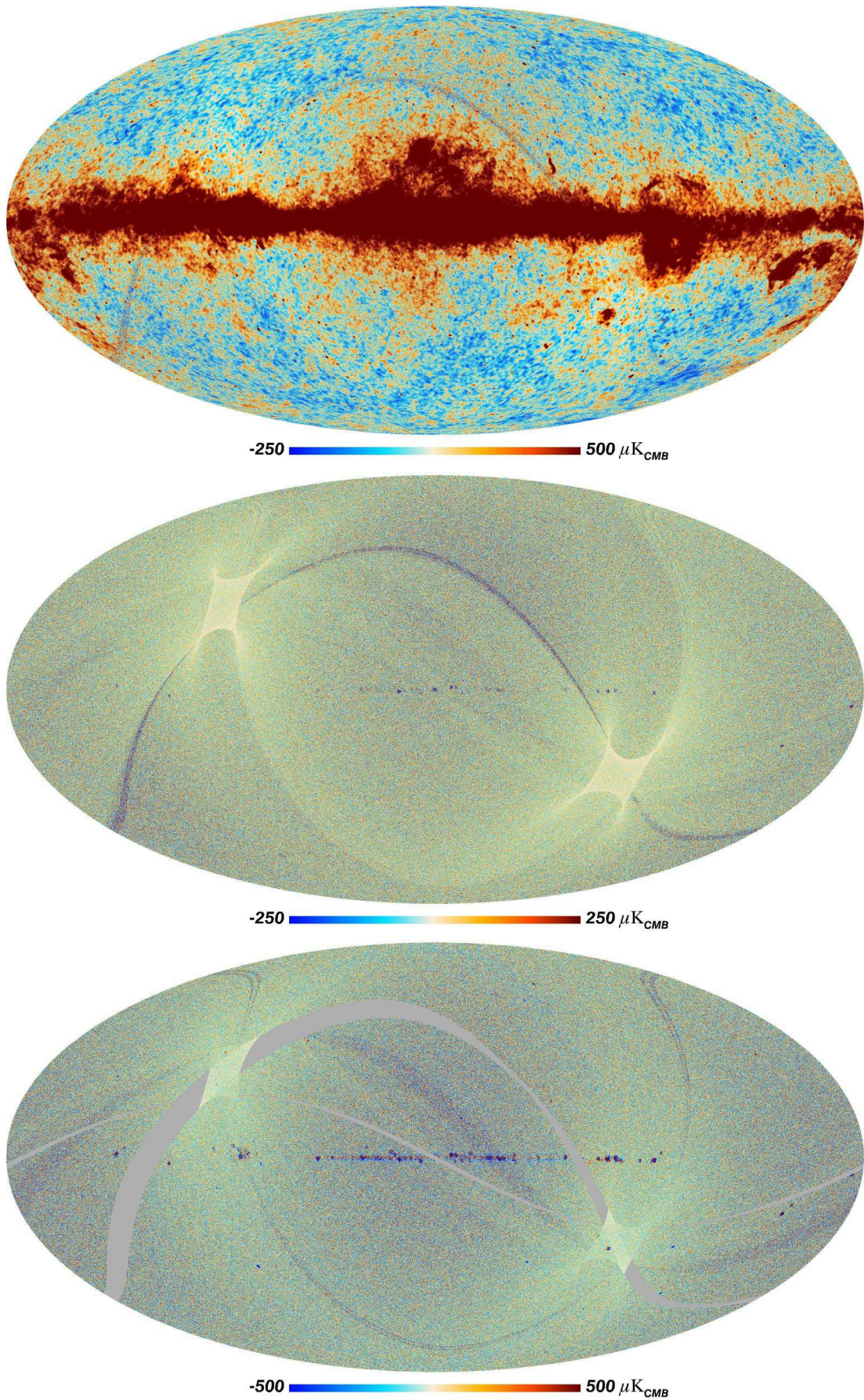
Fig. 8. LFI maps at 30 GHz. The first row gives the intensity expressed in μK_{CMB}. The second row shows the difference between maps made of the first and the second half of each stable pointing period. The third row display the difference between the first and second survey maps.
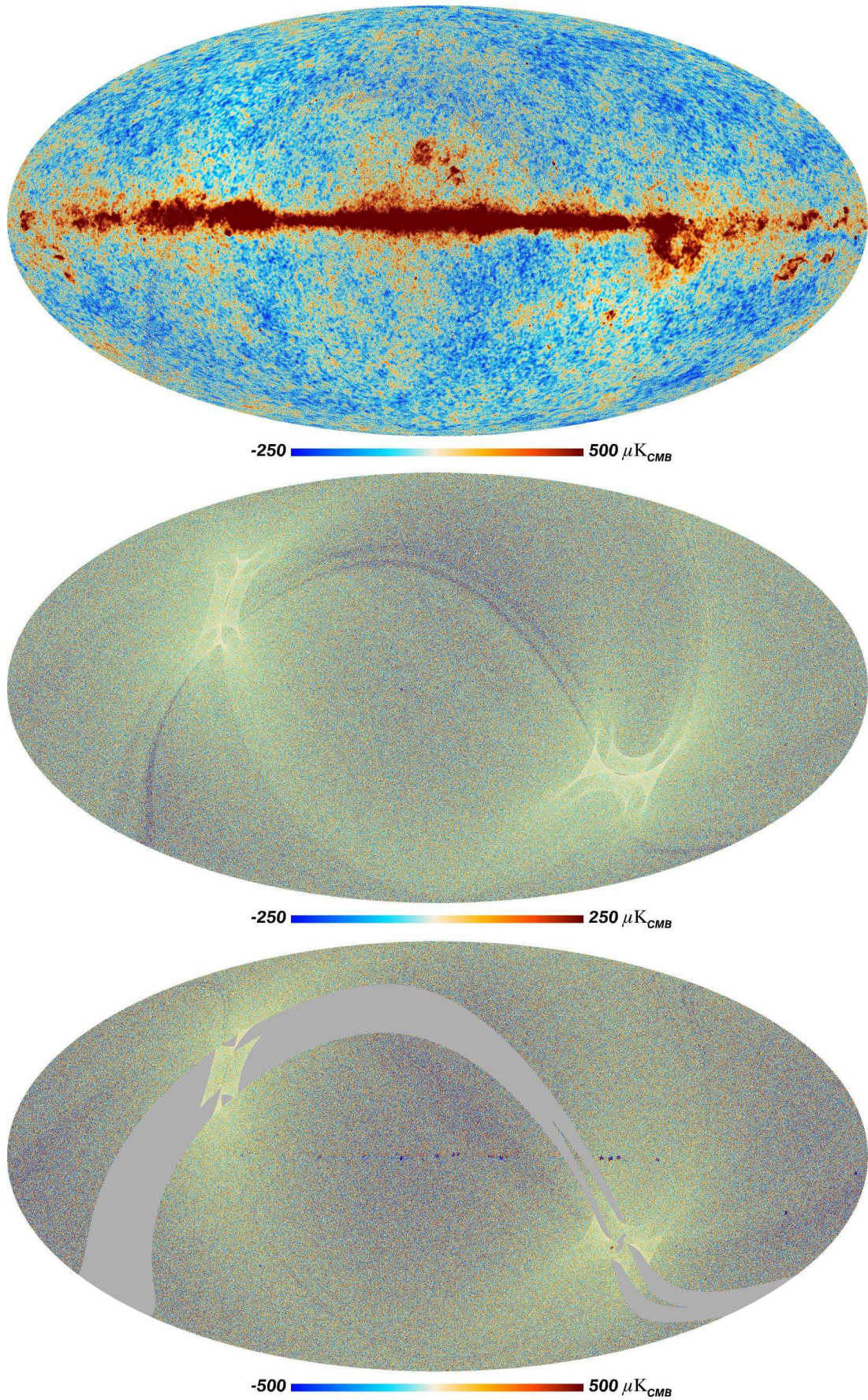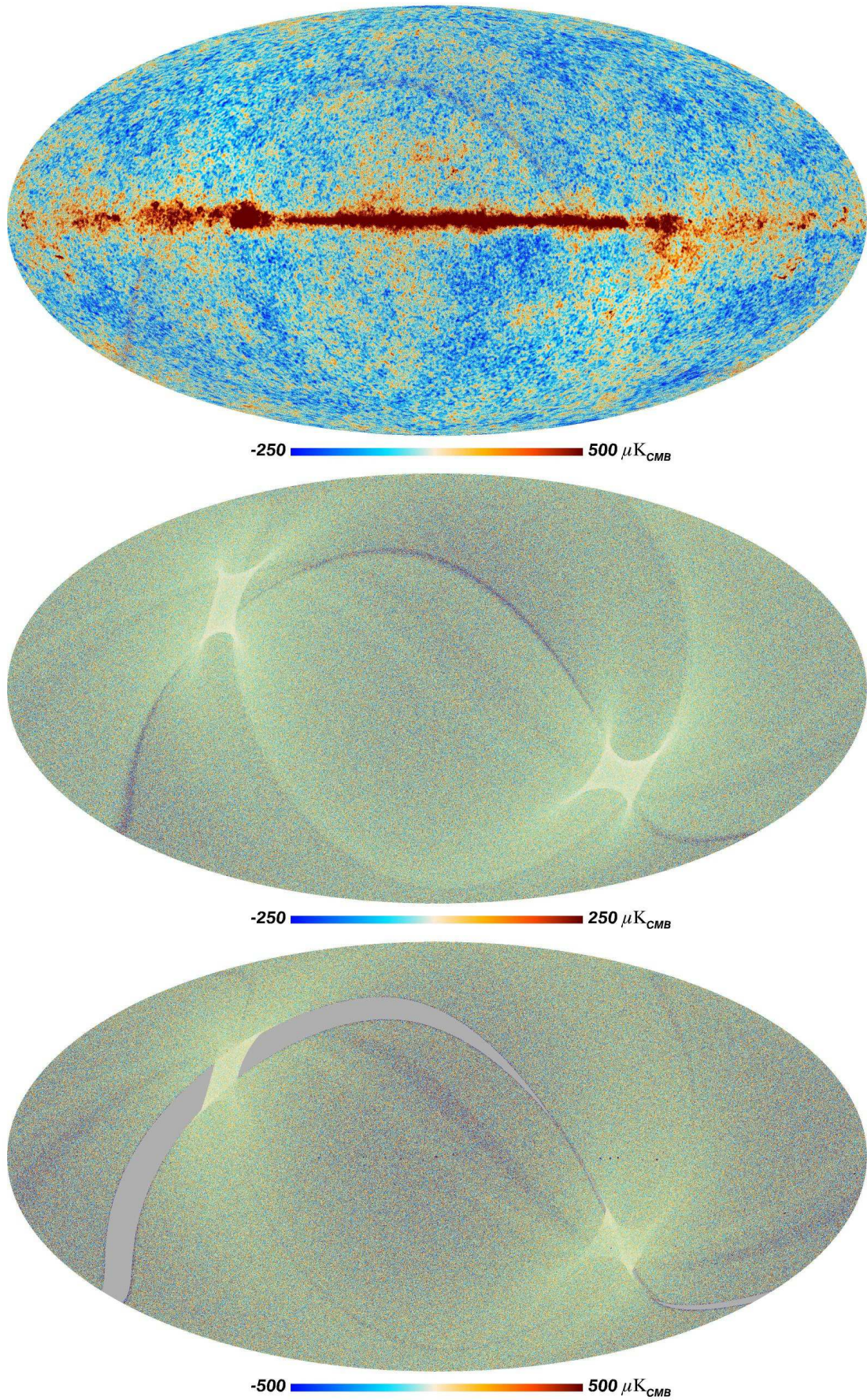
Fig. 9. LFI maps at 44 GHz. The first row gives the intensity expressed in μK_{CMB}. The second row shows the difference between maps made of the first and the second half of each stable pointing period. The third row display the difference between the first and second survey maps.

Fig. 10. LFI maps at 70 GHz. The first row gives the intensity expressed in μK_{CMB}. The second row shows the difference between maps made of the first and the second half of each stable pointing period. The third row display the difference between the first and second survey maps.

cation of the data quality at these multipoles. However at very low-ℓ residuals are present especially at 30 GHz and at 70 GHz and these unable us for a proper characterisation of the cosmological signal.

We have simulated the impact of numerous systematic errors to see if they can explain the observed residuals, including foreground correction, bandpass mismatch, Galactic straylight (i.e., leakage through the far sidelobes), and gain errors. None of these simulations have individually generated artefacts as large as those observed. The most likely candidate seems to be in the combination of far sidelobe correction and calibration errors. As described in Planck Collaboration V (2013), uncertainty in the far sidelobe pattern is one of the dominant contributors to our calibration uncertainty, as well as making our estimates of the additive effect of Galactic straylight quite uncertain.

11. Power Spectra

LFI temperature power spectra are computed from frequency maps using a cROMAster, an implementation of the pseudo-C_ℓ method described in Hivon et al. (2002). We extend it to derive both auto- and cross-power spectra (see Polenta et al. (2005) for a comparison between the two estimators). Noise bias and covariance matrices have been computed through the full focal plane simulations version 6 "FFP6" that include 1000 realization of both signal and noise maps consistent with *Planck* data. The angular response of the instrument is accounted for by using the beam window functions presented in Planck Collaboration IV (2013). Coupling kernels to correct for uncompleted sky coverage are computed as described in Annex. B of Planck Collaboration XV (2013). We have masked the Galactic Plane and point sources using masks described in Sec. 3 of Planck Collaboration XII (2013). In particular, we have used a 70% Galactic mask for 44 and 70 GHz (leaving 70% of the sky uncovered), while we have used a 60% Galactic mask for 30 GHz.

We show in Fig. 11 the 30, 44, and 70 GHz temperature power spectra. These have been produced from frequency maps without performing component separation. Nevertheless, there is a clear agreement between the observed spectra and the *Planck* likelihood code best fit curve (Planck Collaboration XV 2013) when we add a simple foreground component to account for unresolved point source residuals.

12. Data validation

In order to assess and verify the quality of LFI data produced within the data-analysis pipeline, a set of null tests was prepared and performed. The main goal is to validate LFI science data by highlighting possible instrumental systematic effects. These include effects which are either properly corrected or accounted for in the pipeline; or are related to known changes in the operational conditions of the LFI instrument (e.g., the switch over of sorption cooler) or to intrinsic instrument properties coupled to the sky like stray-light from sidelobes. Such tests are also useful for a detailed analysis of the processing steps implemented in the pipeline. Finally, such null tests may discover unanticipated problems (e.g., related to different calibration approaches).

Null tests were carried out on blocks of data on different time scales ranging from pointing periods to one year of observation, and at different unit levels (radiometer, horn, horn-pairs within a given frequency and at frequency level) for both total intensity and, when applicable, for polarization. Such approach is quite demanding in terms of all possible combinations and specific
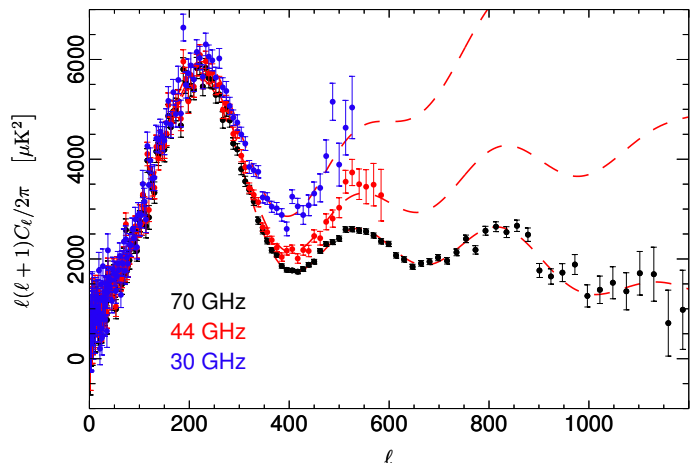
Fig. 11. Temperature power spectra at 30, 44, and 70 GHz. Dashed lines correspond to the *Planck* Likelihood Code best-fit plus a foreground component to account for unresolved point sources.

tools to handle this work-load have been prepared by a dedicated team that creates a parallel code, responsible for both the actual computation of the null-tests and the creation of the output maps and spectra, and the visualization code that creates a report (a HTML page) with all the output from the null tests.

The kind of effects probed by null tests depend on the combination of data and time scale treated. For example, differences at horn level between odd and even number surveys clearly reveal the impact of sidelobes since the sky covered is exactly the same but beam orientation is not. On the other hand, differences between horns for the entire data period may reveal calibration issues and/or changes in the operational or instrumental conditions.

12.1. Null tests summary

It is important also to set a pass-fail criterion for such null tests. In general a failure of a specific test reveals some issue in the data or in the data analysis. These have to be carefully studied and specific actions have to be taken in order to at least mitigate the non ideal result revealed by the test. A simple figure of merit would be the actual level of noise in the data derived from half-ring differences maps. Any departure from the half-ring difference maps noise level would be an indication of some problems. For example (Planck Collaboration III 2013) null test power spectra are used to check the total level of systematic effects in the data. In Fig. 12 we report results at frequency level of survey difference null tests for both TT and EE spectra compared to the noise level derived from half-ring differences maps.

It is worth mentioning that from such results we have carefully analyzed our calibration pipeline and particularly the treatment of sidelobes. This has been corrected, updated with the inclusion of both the intermediate beam as well as the in-band beam behavior based on simulations. This will be the final approach for data calibration in the next release.

Although it is clear from these results that a proper treatment of sidelobes is necessary for final refinements in calibration, it is important to note that the overall amplitude of such effects is well below the CMB signal in total intensity, leaving the analysis of LFI temperature maps totally unaffected.
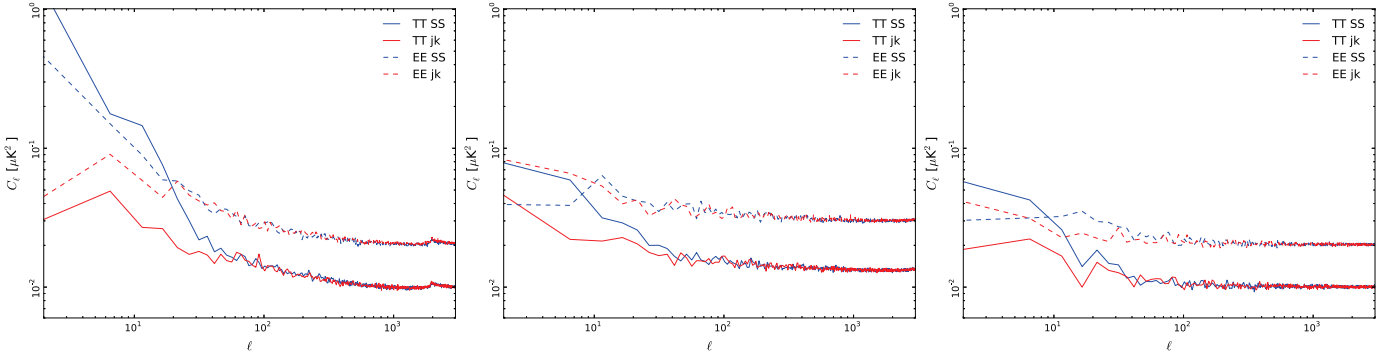
Fig. 12. Null tests results: power spectra from survey difference maps (SS) compared to half-ring difference maps (jk) noise level. Some excess at low multipoles is clearly visible at 30 GHz (*Left*), where the main source has been identified as sidelobe contribution. At 44 (*Centre*) and 70 GHz (*Right*), those null tests provide an indication of less impact of the low-ℓ contribution both in TT and in EE although residuals are still present. For multipoles larger than few tens, null tests EE spectra follow the expected level of noise as traced by half-ring difference.

12.2. Half ring test

The middle panels of Figs. 8, 9, and 10 show the noise calculated from the hit-count-weighted half-ring difference maps at the native $N_{\rm side} = 1024$ resolution, as described by Zacchei et al. (2011) and Planck Collaboration ES (2013). As a first quality check of the maps (and as one of the tests of the whole data processing pipeline up to the maps) we tested both numerically and visually that the noise maps divided pixel-by-pixel by the square root of the white noise covariance maps (see again Planck Collaboration ES (2013)) were approximately Gaussian with rms near to unity; the results were 1.0211, 1.0089, and 1.0007 for 30, 44, and 70 GHz, respectively.

The half-ring difference maps $n_{\rm m}$ are the most direct measure of the noise in the actual maps. The other noise estimates (NCVM and noise Monte Carlo) rely on specific modeling of the noise in the TOD, and this modeling can be validated by comparing the results to the half-ring difference maps. For this purpose we calculated the temperature and polarization (E and B mode) auto-correlation and cross-correlation angular power spectra of the noise by `anafast` using the half-ring difference maps and compared to these the results from the white noise covariance matrices (WNCM) calculated by both `madam` and the noise Monte Carlo simulations (Sect. 9.4). Figure 13 illustrates such a comparison. Further, we calculated the mean C_ℓ for the high-ℓ tails ($\ell = 1150$—1800) of the noise angular power spectra and took the ratio to the WNCM estimate; see Figure 14. As expected, there is some residual $1/f$ noise even in the high-ℓ region, i.e., the full noise MC leads to slightly higher noise prediction than the WNCM or binned white noise from the noise MC. The residual $1/f$ noise is of the order of 2.5% at 30 GHz, 1.0% at 44 GHz, and 0.1% at 70 GHz. Between the noise MC and the direct noise calculation from the half-ring difference maps we find good consistency: the high-ℓ noise from noise MC is only 0.8% higher at 30 GHz, 0.2% higher at 44 GHz and 0.1% lower at 70 GHz than the result from the half-ring difference. It should be noted that the error bars of the noise MC do not include at this stage the uncertainty of noise parameters indicated in Tables 9 and 10. More such comparison are reported in Planck Collaboration ES (2013).

12.3. Intra frequency consistency check

We have tested the consistency between 30, 44, and 70 GHz maps by comparing the power spectra in the multipole range around the first acoustic peak. In order to do so, we have removed the estimated contribution from unresolved point source from the spectra presented in Sec. 11. We have then built the scatter plots for the three frequency pairs, i.e., 70 vs 30 GHz, 70 vs 44 GHz, and 44 vs 30 GHz, and performed a linear fit accounting for errors on both axis.

The results reported in Fig. 15 show that the three power spectra are consistent within the errors. Moreover, please note that current error budget does not account for foreground removal, calibration, and window function uncertainties. Hence, the resulting agreement between spectra at different frequencies can reasonably be considered even more significant. We also compared the flux densities of compact sources at the three LFI frequencies, derived from the PCCS, *Planck* catalogue of compact sources (Planck Collaboration XXVIII 2013) and find these in acceptable agreement. These tests are described briefly in Planck Collaboration XI (2013).

12.4. 70 GHz internal consistency check

We use the Hausman test (Polenta et al. 2005) to assess the consistency of auto and cross spectral estimates at 70 GHz. We define the statistic:

$$H_\ell = \left(\hat{C}_\ell - \tilde{C}_\ell\right) / \sqrt{Var\left\{\hat{C}_\ell - \tilde{C}_\ell\right\}}, \qquad (22)$$

where $\hat{C}_\ell$ and $\tilde{C}_\ell$ represent auto- and cross-spectra, respectively. In order to combine information from different multipoles into a single quantity, we define the following quantity:

$$B_L(r) = \frac{1}{\sqrt{L}} \sum_{\ell=2}^{[Lr]} H_\ell, r \in [0, 1] \qquad (23)$$

where [.] denotes integer part. The distribution of $B_L(r)$ converges (in a functional sense) to a Brownian motion process, which can be studied through the statistics $s_1 = \sup_r B_L(r)$, $s_2 = \sup_r |B_L(r)|$ and $s_3 = \int_0^1 B_L^2(r)dr$. Using the "FFP6" simulations we derive the empirical distribution for all the three test statistics and we then compare them with the results obtained from *Planck* data itself (see Fig. 16). The Hausman test shows no statistically significant inconsistencies between the two spectral estimates.

As a further test, we have estimated the temperature power spectrum for each of three horn-pair map, and we have compared
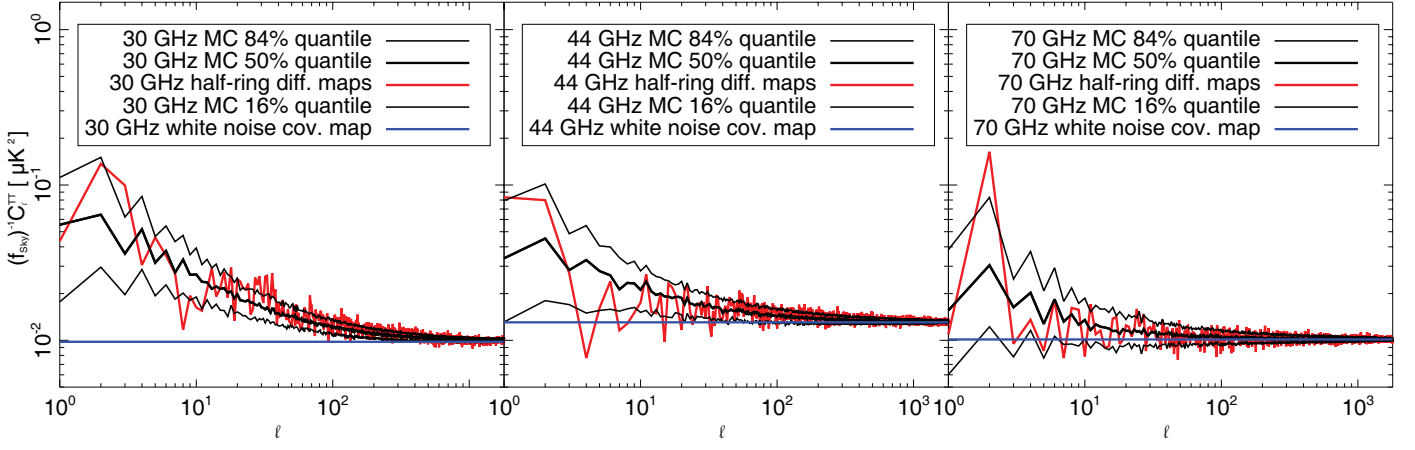
Fig. 13. Comparison of the noise angular power spectra of intensity maps: red from half-ring difference maps, blue from white noise covariance maps produced by `madam`, and black 16%, 50%, and 84% quantiles from noise MC for each C_ℓ. (Note that in the noise MC case no errors were propagated from Tables 9 and 10; only the median values of the three noise parameters were used.)
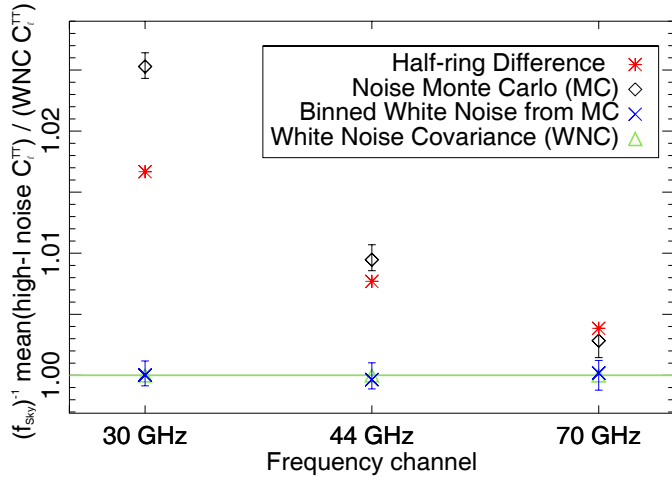

Fig. 14. The ratio of mean noise angular power at high-ℓ ($\ell = 1150$—1800) to the white noise estimate from white noise co-variance matrices: red from the hit-count-weighted half-ring difference, black from 101 full noise Monte Carlo maps, and blue the binned white noise from the noise Monte Carlo. The "reference" white noise levels (green) are 9.8×10^{-15} K^2, 13.1×10^{-15} K^2, and 10.1×10^{-15} K^2, for 30, 44, and 70 GHz, respectively. (Note that in the noise MC no errors were propagated from Tables 9; 10, only the median values of the three noise parameters were used. Therefore the error bars in noise Monte Carlo represent only the statistical variance in 101 simulated noise map realizations. If the uncertainty of the estimation of the three noise parameters was propagated to the noise MC, the error bars would be much larger.)

the results with the spectrum obtained from all 12 radiometers shown above. In Fig. 17 we show the difference between the horn-pair and the combined power spectra. Again, the error bars have been estimated from the "FFP6" simulated dataset. A χ^2 analysis of the residual shows that they are compatible with the null hypothesis, confirming the strong consistency of the estimates.

Table 12. Summary of systematic effects uncertainties on maps[a] in μK_{CMB}.

	30 GHz		44 GHz		70 GHz	
	p-p	rms	p-p	rms	p-p	rms
Bias fluctuations	0.08	0.01	0.10	0.02	0.23	0.06
Thermal fluctuations . . .	0.61	0.11	0.40	0.08	1.17	0.20
1-Hz spikes	0.87	0.17	0.14	0.03	0.60	0.12
Sidelobes pickup	18.95	4.53	1.92	0.57	6.39	1.91
ADC non linearity	3.87	1.01	0.89	0.19	0.92	0.19
Gain residuals	4.33	1.16	4.74	0.97	6.51	1.10
Total	21.02	4.83	5.61	1.13	7.87	2.00

[a] Calculated on a pixel size approximately equal to the average beam FWHM.

12.5. Updated systematic effects assessment

Analysis of know systematic effects in *Planck* LFI is reported in detail in Planck Collaboration III (2013). Here we include only the summary Table 12 where we list the r.m.s. and the difference between the 99% and the 1% quantiles in the pixel value distributions. For simplicity we refer to this difference as peak-to-peak (p-p) difference, even though it neglects outliers. It nevertheless effectively approximates the peak-to-peak variation of the effect on the map.

Our analysis (Planck Collaboration III 2013) has shown that systematic effect uncertainties, are at least two orders of magnitudes below the CMB temperature anisotropy power spectrum and are dominated by straylight pick-up from far sidelobes and imperfect photometric calibration.

13. Infrastructure Overview

The computer cluster used for the maps production consists of two types of nodes: ten 64 bit nodes with two single-core CPUs and 16 GB of RAM, and ten 64 bit nodes containing two motherboards, each equipped with two six-cores CPUs and 72 GB of RAM. The total RAM available exceeds 1.5 TB, a sufficient
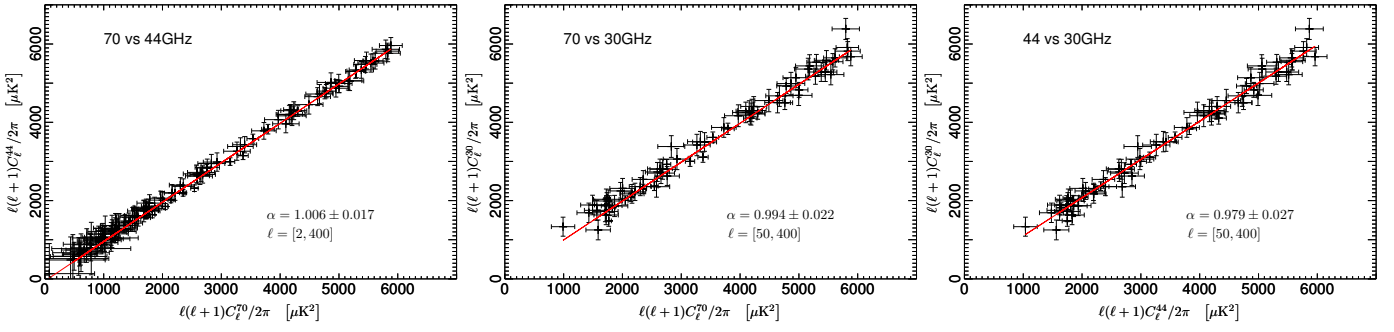
Fig. 15. Consistency between estimates of the angular power spectra at frequencies. From *Left* to *Right*: 70 vs 44 GHz; 70 vs 30 GHz; 44 vs 30 GHz. Solid red lines are the best fit of the linear regressions, whose angular coefficients α are consistent with unity within the errors.
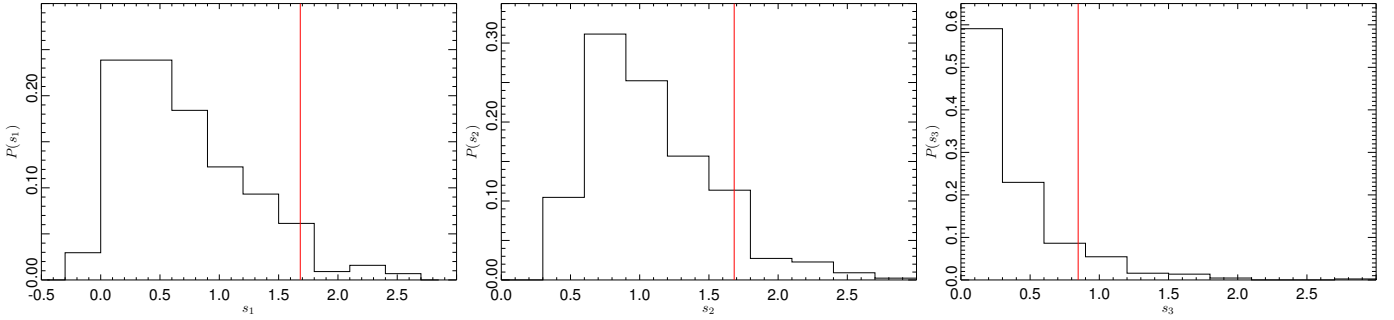
Fig. 16. From *Left* to *Right*, the empirical distribution (estimated via "FFP6") of the s_1, s_2, s_3 statistics (see text). The vertical line represents 70 GHz data.

quantity to allow for the creation of all the maps until the end of the mission. The dual-motherboard nodes are connected through an infiniband network interface (40 Gbit), while an 1 Gbit interface is provided for the other connections.

The hardware infrastructure includes a front-end (two quad-core CPUs, 8 GB of RAM), which is the access point for the users and hosts the pbs server, and a control machine running the LDAP authentication server and the DNS and DHCP services.

The software used for the system management and synchronization includes tools as `kickstart` and `puppet`, while the parallelization of the computation is guaranteed by the `torque` resource manager and the `maui` scheduler.

Data products are stored and organized into three different servers that host the Level 1, Level 2 and test databases (Fig. 1. For each of these databases there is an associated RAID 6 storage with up to 40 TB formatted with the JFS filesystem.

14. Discussion and Conclusions

We have described the pipeline used to process the *Planck*/LFI data, starting from Level 1 continuing the production of the temperature frequency maps based on the first 15.5 months of observations. Furthermore, we have described the strategy for the verification of the quality of the products, which is largely based on null tests. Due to the complexity of the analysis process, three companion papers provide detail on specific critical aspects of the data analysis and products delivered: Planck Collaboration III (2013) reports the analysis on systematic effects and assessment of their impact; Planck Collaboration V (2013) describes in detail the photometric calibration (approaches and testing); Planck Collaboration IV (2013) outlines the determination of the LFI beam patterns and window functions. In addition, the *Planck*

explanatory document Planck Collaboration ES (2013) provides a detailed description of all the products delivered in this release.

The entire Level 1 pipeline was unchanged since the start of the mission (about four years ago) and has been running flawlessly and continuously, demonstrating the robustness of the design and development approach. IN contrast, the Level 2 pipeline was largely restructured; see Zacchei et al. (2011) for a description of the initial pipeline. The major improvements involved new procedures for pointing reconstruction, detailed estimation of systematic effects and photometric calibration. These improvements allowed us to obtain, as reported in Table 1, a final calibration uncertainty of the order of 0.6%, and also to propagate, using simulations, known systematic effects into the final product maps. The impact of the combination of all systematic effects has been evaluated to be at least two orders of magnitudes below the CMB temperature anisotropy power spectrum.

Particular emphasis was given to null tests, which were routinely applied to various subsets of the data, in order to quantitatively assess the scientific quality of the LFI products. The null test procedure, described in Sec. 12, allowed us to detect and solve a number of problems in the implementation of our pipeline, which emerged during the processing period. In fact, the pipeline is still being optimized and more improvements are planned for the next data release. Future improvements of Level 2 will be aimed at obtaining high-quality polarization results, which require control of spurious effects at sub-μK level. We are also concentrating our effort on a better beam characterization that takes in account second order effects – such as the bandpass response of each diode, or Galactic straylight (i.e., leakage through the far sidelobes) – during the calibration process. These and other refinements are being included in the LFI pipeline to meet the level of accuracy needed for a robust analysis of polarization data.
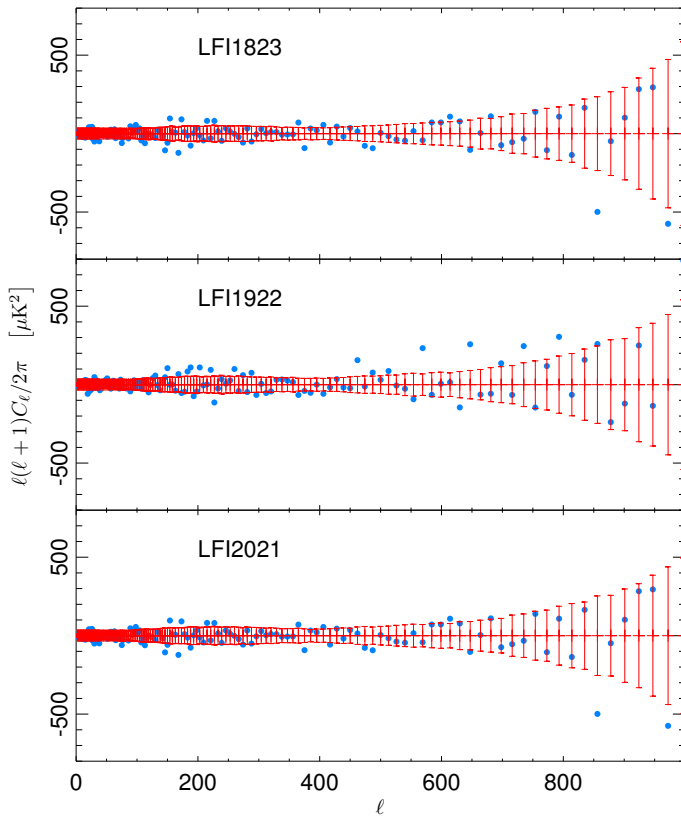
Fig. 17. Residuals between the auto power spectra of the horn pair maps and the power spectrum of the full 70 GHz frequency map. Error bars are derived from "FFP6" simulations.

References

Bersanelli, M., Mandolesi, N., Butler, R. C., et al. 2010, A&A, 520, A4+
de Gasperis, G., Balbi, A., Cabella, P., Natoli, P., & Vittorio, N. 2005, A&A, 436, 1159
Górski, K. M., Hivon, E., Banday, A. J., et al. 2005, ApJ, 622, 759
Hinshaw, G., Weiland, J. L., Hill, R. S., et al. 2009, ApJS, 180, 225
Hivon, E., Górski, K. M., Netterfield, C. B., et al. 2002, ApJ, 567, 2
Keihänen, E., Keskitalo, R., Kurki-Suonio, H., Poutanen, T., & Sirviö, A. 2010, A&A, 510, A57+
Keskitalo, R., Ashdown, M., Cabella, P., et al. 2010, Astron.Astrophys., 522, A94
Leahy, J. P., Bersanelli, M., D'Arcangelo, O., et al. 2010, A&A, 520, A8+
Mennella, A., Bersanelli, M., Butler, R. C., et al. 2010, A&A, 520, A5+
Mennella, A., Bersanelli, M., Seiffert, M., et al. 2003, A&A, 410, 1089
Mennella, A., Butler, R. C., Curto, A., et al. 2011, A&A, 536, A3
Mitra, S., Rocha, G., Górski, K. M., et al. 2011, ApJS, 193, 5
Natoli, P., de Gasperis, G., Gheller, C., & Vittorio, N. 2001, A&A, 372, 346
Planck Collaboration. 2011, The Explanatory Supplement to the Planck Early Release Compact Source Catalogue (ESA)
Planck Collaboration ES. 2013, The Explanatory Supplement to the Planck 2013 results (ESA)
Planck Collaboration I. 2011, A&A, 536, A1
Planck Collaboration I. 2013, Submitted to A&A
Planck Collaboration II. 2011, A&A, 536, A2
Planck Collaboration III. 2013, Submitted to A&A
Planck Collaboration IV. 2013, Submitted to A&A
Planck Collaboration IX. 2011, A&A, 536, A9
Planck Collaboration IX. 2013, Submitted to A&A
Planck Collaboration V. 2013, Submitted to A&A
Planck Collaboration VII. 2011, A&A, 536, A7
Planck Collaboration VIII. 2011, A&A, 536, A8
Planck Collaboration X. 2011, A&A, 536, A10
Planck Collaboration XI. 2011, A&A, 536, A11
Planck Collaboration XI. 2013, Submitted to A&A
Planck Collaboration XII. 2011, A&A, 536, A12
Planck Collaboration XII. 2013, Submitted to A&A
Planck Collaboration XIII. 2011, A&A, 536, A13
Planck Collaboration XIV. 2011, A&A, 536, A14
Planck Collaboration XIX. 2011, A&A, 536, A19
Planck Collaboration XV. 2011, A&A, 536, A15
Planck Collaboration XV. 2013, Submitted to A&A
Planck Collaboration XVI. 2011, A&A, 536, A16
Planck Collaboration XVII. 2011, A&A, 536, A17
Planck Collaboration XVIII. 2011, A&A, 536, A18
Planck Collaboration XX. 2011, A&A, 536, A20
Planck Collaboration XXI. 2011, A&A, 536, A21
Planck Collaboration XXII. 2011, A&A, 536, A22
Planck Collaboration XXIII. 2011, A&A, 536, A23
Planck Collaboration XXIII. 2013, Submitted to A&A
Planck Collaboration XXIV. 2011, A&A, 536, A24
Planck Collaboration XXV. 2011, A&A, 536, A25
Planck Collaboration XXVIII. 2013, Submitted to A&A
Planck HFI Core Team. 2011a, A&A, 536, A4
Planck HFI Core Team. 2011b, A&A, 536, A6
Polenta, G., Marinucci, D., Balbi, A., et al. 2005, Journal of Cosmology and Astro-Particle Physics, 11, 1
Prunet, S., Ade, P. A. R., Bock, J. J., et al. 2001, ArXiv Astrophysics e-prints
Reinecke, M., Dolag, K., Hell, R., Bartelmann, M., & Enßlin, T. A. 2006, A&A, 445, 373
Seiffert, M., Mennella, A., Burigana, C., et al. 2002, A&A, 391, 1185
Tauber, J. A., Norgaard-Nielsen, H. U., Ade, P. A. R., et al. 2010, A&A, 520, A2+

Zacchei, A., Maino, D., Baccigalupi, C., et al. 2011, A&A, 536, A5

Zonca, A., Franceschet, C., Battaglia, P., et al. 2009, Journal of Instrumentation, 4, 2010

[1] APC, AstroParticule et Cosmologie, Université Paris Diderot, CNRS/IN2P3, CEA/lrfu, Observatoire de Paris, Sorbonne Paris Cité, 10, rue Alice Domon et Léonie Duquet, 75205 Paris Cedex 13, France

[2] Aalto University Metsähovi Radio Observatory, Metsähovintie 114, FIN-02540 Kylmälä, Finland

[3] African Institute for Mathematical Sciences, 6-8 Melrose Road, Muizenberg, Cape Town, South Africa

[4] Agenzia Spaziale Italiana Science Data Center, c/o ESRIN, via Galileo Galilei, Frascati, Italy

[5] Agenzia Spaziale Italiana, Viale Liegi 26, Roma, Italy

[6] Astrophysics Group, Cavendish Laboratory, University of Cambridge, J J Thomson Avenue, Cambridge CB3 0HE, U.K.

[7] CITA, University of Toronto, 60 St. George St., Toronto, ON M5S 3H8, Canada

[8] CNR - ISTI, Area della Ricerca, via G. Moruzzi 1, Pisa, Italy

[9] CNRS, IRAP, 9 Av. colonel Roche, BP 44346, F-31028 Toulouse cedex 4, France

[10] California Institute of Technology, Pasadena, California, U.S.A.

[11] Centre for Theoretical Cosmology, DAMTP, University of Cambridge, Wilberforce Road, Cambridge CB3 0WA U.K.

[12] Centro de Estudios de Física del Cosmos de Aragón (CEFCA), Plaza San Juan, 1, planta 2, E-44001, Teruel, Spain

[13] Computational Cosmology Center, Lawrence Berkeley National Laboratory, Berkeley, California, U.S.A.

[14] Consejo Superior de Investigaciones Científicas (CSIC), Madrid, Spain

[15] DSM/Irfu/SPP, CEA-Saclay, F-91191 Gif-sur-Yvette Cedex, France

[16] DTU Space, National Space Institute, Technical University of Denmark, Elektrovej 327, DK-2800 Kgs. Lyngby, Denmark

[17] Département de Physique Théorique, Université de Genève, 24, Quai E. Ansermet,1211 Genève 4, Switzerland

[18] Departamento de Física Fundamental, Facultad de Ciencias, Universidad de Salamanca, 37008 Salamanca, Spain

[19] Departamento de Física, Universidad de Oviedo, Avda. Calvo Sotelo s/n, Oviedo, Spain

[20] Departamento de Matemáticas, Estadística y Computación, Universidad de Cantabria, Avda. de los Castros s/n, Santander, Spain

[21] Department of Astronomy and Astrophysics, University of Toronto, 50 Saint George Street, Toronto, Ontario, Canada

[22] Department of Astrophysics/IMAPP, Radboud University Nijmegen, P.O. Box 9010, 6500 GL Nijmegen, The Netherlands

[23] Department of Electrical Engineering and Computer Sciences, University of California, Berkeley, California, U.S.A.

[24] Department of Physics & Astronomy, University of British Columbia, 6224 Agricultural Road, Vancouver, British Columbia, Canada

[25] Department of Physics and Astronomy, Dana and David Dornsife College of Letter, Arts and Sciences, University of Southern California, Los Angeles, CA 90089, U.S.A.

[26] Department of Physics and Astronomy, University College London, London WC1E 6BT, U.K.

[27] Department of Physics, Gustaf Hällströmin katu 2a, University of Helsinki, Helsinki, Finland

[28] Department of Physics, Princeton University, Princeton, New Jersey, U.S.A.

[29] Department of Physics, University of California, One Shields Avenue, Davis, California, U.S.A.

[30] Department of Physics, University of California, Santa Barbara, California, U.S.A.

[31] Department of Physics, University of Illinois at Urbana-Champaign, 1110 West Green Street, Urbana, Illinois, U.S.A.

[32] Dipartimento di Fisica e Astronomia G. Galilei, Università degli Studi di Padova, via Marzolo 8, 35131 Padova, Italy

[33] Dipartimento di Fisica e Scienze della Terra, Università di Ferrara, Via Saragat 1, 44122 Ferrara, Italy

[34] Dipartimento di Fisica, Università La Sapienza, P. le A. Moro 2, Roma, Italy

[35] Dipartimento di Fisica, Università degli Studi di Milano, Via Celoria, 16, Milano, Italy

[36] Dipartimento di Fisica, Università degli Studi di Trieste, via A. Valerio 2, Trieste, Italy

[37] Dipartimento di Fisica, Università di Roma Tor Vergata, Via della Ricerca Scientifica, 1, Roma, Italy

[38] Discovery Center, Niels Bohr Institute, Blegdamsvej 17, Copenhagen, Denmark

[39] Dpto. Astrofísica, Universidad de La Laguna (ULL), E-38206 La Laguna, Tenerife, Spain

[40] European Space Agency, ESAC, Planck Science Office, Camino bajo del Castillo, s/n, Urbanización Villafranca del Castillo, Villanueva de la Cañada, Madrid, Spain

[41] European Space Agency, ESTEC, Keplerlaan 1, 2201 AZ Noordwijk, The Netherlands

[42] Haverford College Astronomy Department, 370 Lancaster Avenue, Haverford, Pennsylvania, U.S.A.

[43] Helsinki Institute of Physics, Gustaf Hällströmin katu 2, University of Helsinki, Helsinki, Finland

[44] INAF - Osservatorio Astrofisico di Catania, Via S. Sofia 78, Catania, Italy

[45] INAF - Osservatorio Astronomico di Padova, Vicolo dell'Osservatorio 5, Padova, Italy

[46] INAF - Osservatorio Astronomico di Roma, via di Frascati 33, Monte Porzio Catone, Italy

[47] INAF - Osservatorio Astronomico di Trieste, Via G.B. Tiepolo 11, Trieste, Italy

[48] INAF/IASF Bologna, Via Gobetti 101, Bologna, Italy

[49] INAF/IASF Milano, Via E. Bassini 15, Milano, Italy

[50] INFN, Sezione di Bologna, Via Irnerio 46, I-40126, Bologna, Italy

[51] INFN, Sezione di Roma 1, Università di Roma Sapienza, Piazzale Aldo Moro 2, 00185, Roma, Italy

[52] IPAG: Institut de Planétologie et d'Astrophysique de Grenoble, Université Joseph Fourier, Grenoble 1 / CNRS-INSU, UMR 5274, Grenoble, F-38041, France

[53] ISDC Data Centre for Astrophysics, University of Geneva, ch. d'Ecogia 16, Versoix, Switzerland

[54] IUCAA, Post Bag 4, Ganeshkhind, Pune University Campus, Pune 411 007, India

[55] Imperial College London, Astrophysics group, Blackett Laboratory, Prince Consort Road, London, SW7 2AZ, U.K.

[56] Infrared Processing and Analysis Center, California Institute of Technology, Pasadena, CA 91125, U.S.A.

[57] Institut Néel, CNRS, Université Joseph Fourier Grenoble I, 25 rue des Martyrs, Grenoble, France

[58] Institut Universitaire de France, 103, bd Saint-Michel, 75005, Paris, France

[59] Institut d'Astrophysique Spatiale, CNRS (UMR8617) Université Paris-Sud 11, Bâtiment 121, Orsay, France

[60] Institut d'Astrophysique de Paris, CNRS (UMR7095), 98 bis Boulevard Arago, F-75014, Paris, France

[61] Institute for Space Sciences, Bucharest-Magurale, Romania

[62] Institute of Astronomy and Astrophysics, Academia Sinica, Taipei, Taiwan

[63] Institute of Astronomy, University of Cambridge, Madingley Road, Cambridge CB3 0HA, U.K.

[64] Institute of Theoretical Astrophysics, University of Oslo, Blindern, Oslo, Norway

[65] Instituto de Astrofísica de Canarias, C/Vía Láctea s/n, La Laguna, Tenerife, Spain

[66] Instituto de Física de Cantabria (CSIC-Universidad de Cantabria), Avda. de los Castros s/n, Santander, Spain

[67] Istituto di Fisica del Plasma, CNR-ENEA-EURATOM Association, Via R. Cozzi 53, Milano, Italy

[68] Jet Propulsion Laboratory, California Institute of Technology, 4800 Oak Grove Drive, Pasadena, California, U.S.A.

[69] Jodrell Bank Centre for Astrophysics, Alan Turing Building, School of Physics and Astronomy, The University of Manchester, Oxford Road, Manchester, M13 9PL, U.K.

[70] Kavli Institute for Cosmology Cambridge, Madingley Road, Cambridge, CB3 0HA, U.K.

[71] LAL, Université Paris-Sud, CNRS/IN2P3, Orsay, France

[72] LERMA, CNRS, Observatoire de Paris, 61 Avenue de l'Observatoire, Paris, France

[73] Laboratoire AIM, IRFU/Service d'Astrophysique - CEA/DSM - CNRS - Université Paris Diderot, Bât. 709, CEA-Saclay, F-91191 Gif-sur-Yvette Cedex, France

[74] Laboratoire Traitement et Communication de l'Information, CNRS (UMR 5141) and Télécom ParisTech, 46 rue Barrault F-75634 Paris Cedex 13, France

[75] Laboratoire de Physique Subatomique et de Cosmologie, Université Joseph Fourier Grenoble I, CNRS/IN2P3, Institut National Polytechnique de Grenoble, 53 rue des Martyrs, 38026 Grenoble cedex, France

[76] Laboratoire de Physique Théorique, Université Paris-Sud 11 & CNRS, Bâtiment 210, 91405 Orsay, France

[77] Lawrence Berkeley National Laboratory, Berkeley, California, U.S.A.

[78] Max-Planck-Institut für Astrophysik, Karl-Schwarzschild-Str. 1, 85741 Garching, Germany

[79] McGill Physics, Ernest Rutherford Physics Building, McGill University, 3600 rue University, Montréal, QC, H3A 2T8, Canada

[80] MilliLab, VTT Technical Research Centre of Finland, Tietotie 3, Espoo, Finland

[81] Niels Bohr Institute, Blegdamsvej 17, Copenhagen, Denmark

[82] Observational Cosmology, Mail Stop 367-17, California Institute of Technology, Pasadena, CA, 91125, U.S.A.

[83] SB-ITP-LPPC, EPFL, CH-1015, Lausanne, Switzerland

[84] SISSA, Astrophysics Sector, via Bonomea 265, 34136, Trieste, Italy

[85] School of Physics and Astronomy, Cardiff University, Queens Buildings, The Parade, Cardiff, CF24 3AA, U.K.

[86] School of Physics and Astronomy, University of Nottingham, Nottingham NG7 2RD, U.K.

[87] Space Sciences Laboratory, University of California, Berkeley, California, U.S.A.

[88] Special Astrophysical Observatory, Russian Academy of Sciences, Nizhnij Arkhyz, Zelenchukskiy region, Karachai-Cherkessian Republic, 369167, Russia

[89] Stanford University, Dept of Physics, Varian Physics Bldg, 382 Via Pueblo Mall, Stanford, California, U.S.A.

[90] Sub-Department of Astrophysics, University of Oxford, Keble Road, Oxford OX1 3RH, U.K.

[91] Theory Division, PH-TH, CERN, CH-1211, Geneva 23, Switzerland

[92] UPMC Univ Paris 06, UMR7095, 98 bis Boulevard Arago, F-75014, Paris, France

[93] Université de Toulouse, UPS-OMP, IRAP, F-31028 Toulouse cedex 4, France

[94] Universities Space Research Association, Stratospheric Observatory for Infrared Astronomy, MS 232-11, Moffett Field, CA 94035, U.S.A.

[95] University of Granada, Departamento de Física Teórica y del Cosmos, Facultad de Ciencias, Granada, Spain

[96] University of Miami, Knight Physics Building, 1320 Campo Sano Dr., Coral Gables, Florida, U.S.A.

[97] Warsaw University Observatory, Aleje Ujazdowskie 4, 00-478 Warszawa, Poland